

University of Oxford

Department of Engineering Science

Wadham College

Thesis for the degree of

Masters of Science by Research in Engineering Science

Titled

Moving-mask volume growing: A novel volume segmentation algorithm for medical images.

Dr. Daniel Zajarias-Fainsod MBBS MSc

Abstract

Various physiological modelling studies require isolating the anatomy of interest from medical imaging. There exist a variety of segmentation algorithms, each particularly tailored for a specific anatomical region, imaging modality or physiological modelling study. Simulations of blood flow in brain vasculature require that the arterial and venous vasculature be isolated from angiographic modalities such as rotational planar angiography, computer tomography angiography and magnetic resonance angiography studies. Due to the tortuousity and apposition of the cerebral vessels to the highly vascular meninges and cranium, segmentation of these vessels is generally difficult. This work focuses on a novel algorithm for anatomy segmentation for specific use in the isolation of a particular region of the cerebrovascular anatomy associated with vessel pathology such as aneurysms and arteriovenous malformations. The algorithm uses geometric volume growing by means of comparing the intensities of neighbouring voxels originating from a user-determined seed point rather than fully automated segmentation by means of statistical algorithms that erroneously assume a normal distribution of intensity values in the image data. The research carried out shows that this novel algorithm can easily be incorporated into a simple processing chain for transoperative use by clinicians as the total time from a DICOM stack being imported to a STL geometry being created was on average under 5 minutes. Measurements carried out by clinicians of the anatomy in imaging data strongly correlate with the same measurements on the segmented volumes indicating high accuracy and precision in segmentation. In conclusion, although this algorithm is not suitable for all anatomies, modalities or applications, it shows promise for cerebrovascular studies in particular those where computer fluid dynamics or finite element method

simulations of treatment are carried out. Further work should focus on improvements and tailoring the algorithm for other specific data and applications.

Acknowledgments

The completion of this work would not be possible without the support and encouragement of a few people. Prof. Alfonso Castrejon-Pita deserves the most mention for having stepped up to fill the vacant position and daunting task of being my supervisor. You went above and beyond the call of duty both as supervisor and a friend. Dr. Caroline Mawson also deserves praise; than you for your continuing encouragement and support. To Prof. Alexander Ritter for his helping a medic dabble with the complicated mathematics found in this work. Prof. James Byrne for allowing me to shadow him and the ongoing tutelage he has shown me over the past nine years and introducing me to the wonderful field that is interventional neuroradiology and Dr. Alex Berenstein for being his protégé in this wonderful field. Prof. Yiannis Ventikos, for being my original supervisor and having welcomed me to your research group and giving me the opportunity to come back to the wonderful place that is Oxford.

Without the motivation I received from my friends Margarita Vaysman, Diana Greenwald, Katia Mandaltsi and Alisa Selimovic completing this project would have not been possible. Having met you and calling you my best friends is priceless.

As ever, my family deserves the highest praise for their love and supporting me in all my endeavours. My mother Tamara for always believing in me, my father Guillermo for always providing constructive criticism followed by encouragement, and my brother Robbie for his unconditional support. To my grandparents, for the lessons they taught me and inspiration they gave me. Nico, Abu and Moy, I will always remember you fondly; Ita, whom I love and cherish every moment we spend together. Victor, for being always there no matter the time or place; you are like a second father to us. Mantina, Jose Ramon, Jos, Mat and Juli, for being my other family and for welcoming me to a loving home always.

Lastly I want to thank the Consejo Nacional de Ciencia y Tecnología for the honour and privilege of becoming their scholar and the financial support I received throughout.

Table of Contents

Abstract **1**
Acknowledgments **3**
Table of Contents **5**
Chapter 1: Introduction **6**
Imaging Modalities 9
Plain film radiography 9
Conventional Tomography 11
Computed Tomography (CT) 11
Magnetic Resonance Imaging (MRI) 12
Angiography 13
CT Angiography 16
Magnetic Resonance Angiography (MRA) 16
3D Rotational Angiography 18
Ultrasonography 19
Post-Processing of Digital Images 20
Segmentation 21
Cerebrovascular Disease, Imaging and Segmentation 22
Imaging & 3D Modelling 30
Chapter 2: Data Selection and Pre-Segmentation Processing **35**
Selection of Cases and Image Acquisition Modality 35
Creation of Voxel Geometry 37
Windowing Enhancement 39
Cropping and File Size Reduction 41
Chapter 3: Segmentation **43**
Background 43
Two-dimensional image segmentation 45
Segmentation by volume growing algorithm 51
Segmentation by volume growing algorithm 57
Meshing of segmented volume 60
Accuracy test for segmentation algorithm 62
Chapter 4: Discussion & Conclusion **64**
Chapter 5: Bibliography **67**
Appendix A: MatLab Code **74**
DICOM Load 74
Enhance (Thresholding) 74
Cropping 76
Segmentation (Moving-Mask Volume Growing) 77
Finer Voxels 78
Smoothing 78

Chapter 1: Introduction

Since the beginning of medical diagnosis and treatment, people have attempted to look inside the body without causing damage. The medical specialism of pathology specialises in the study of disease. This is usually done by observation at the macroscopic level which includes the organs as well as at the microscopic level where tissues and cells are observed. Dissections and autopsies have been common throughout history in various cultures [1], however they are not normally possible in the live subject, hence a diagnosis carried out by such invasive observation was carried out either postmortem or otherwise was likely to cause death. At later points in the history of medicine, there have been numerous attempts to delve into the workings of the human body without causing harm. Of note is Anton Mesmer, who with his theories of 'animal magnetism' claimed to be able to sense disease and corruption within the body by simply waving his hands over the patient [2]. Although this was nothing more than sensationalism, and at best can be credited as an instance of hypnotherapy, it clearly shows the need for imaging the internal anatomy for accurate diagnosis. One of the earliest methods of imaging is transluminescence, a practice that involves shining a strong light source through a relatively thin body part in order to differentiate internal structures that have a different opacity to light. Such a practice was only useful for body parts such as the hands, particularly of younger or lean subjects, where viewing was carried out by using a tube or pipe impervious to light. The observer would press one end to the body part of interest and would view towards the sun through the opposite end [1]. By means of transluminescence it is possible to discern structures such as bone —and in some cases fractures—, blood vessels and growths. It is important to note that transluminescence is still employed today by physicians to view body structures such as the scrota and testicles as well as

[1] This chapter contains sections adapted from previous unpublished work by Daniel Zajarias-Fainsod at the University of Warwick in 2010.

phalanges; nevertheless, the modern practice involves the use of a pen torch rather than the sun [3].

It was not until the discovery of X-rays that true imaging became possible. Although misunderstood and at times vilified, X-rays have revolutionised not only medical diagnosis but treatment as well. The story of the discovery of X-rays' utility in medical imaging can be typified by the story of Anna Bertha, Wilhelm Röntgen's wife, who exclaimed "I have seen my death!", upon seeing the skeleton of her hand in one of her husband's first uses of X-rays for anatomical visualisation. Only a couple weeks earlier, on the 8th of November, 1885, Dr. Röntgen generated X-rays and discovered some of their remarkable properties [4]. Like most scientific discoveries, the possible application of X-rays to medical imaging was serendipity. While experimenting with the new rays and how they affect different materials he saw the shadow of his skeleton on a barium platinocyanide screen he had placed to fluoresce under the exposure of his X-rays. Röntgen went on to win the first Nobel Price in Physics and inspired a completely new field of medicine [5].

Since the first Röntgenograms, medical imaging has advanced significantly; nonetheless, X-rays still account for the most common method or modality of image acquisition. Various other modalities apart from simple planar radiograms—as Röntgenograms are now referred to—use X-rays including computed tomography (CT) scans and many types of angiography. Other methods have since been discovered that provide medical images of great value including ultrasound sonography and nuclear magnetic resonance imaging (MRI). These and many other modalities have revolutionised medicine allowing physicians not only to peer inside the body but also to guide various therapies.

In fact, a branch of medicine called interventional radiology not only relies on imaging but would not exist without it. This form of medical treatment involves minimum-invasive techniques using precise imaging to guide a variety of tools to treat numerous pathologies in different organs. One of the most significant uses of this technology is done in the field of interventional neuroradiology, also known as endovascular brain surgery, where catheters are inserted into the inguinal arteries and guided with imaging toward the cranial vault through the arterial tree. Endovascular methods are employed in the treatment of thromboembolic stroke, cerebral aneurysms, arteriovenous malformations and tumours to name just a few [6]. It permits quick access to the affected area, with minimal preparation, less collateral damage, lower risk of infection and haemodynamic instability as well as a faster recovery time than conventional surgery [7]. Although for each one of these pathologies the endovascular surgeon will require a wide array of instrumentation, what remains a constant is the use of an imaging technique. This is due to the indispensable necessity of visualisation of the blood vessels so that the interventionist may advance catheters and wires from the point of entry through to the location where the interventional procedure will be carried out. For purposes of literary simplicity and due to the nature and purpose of this review, mention of aneurysms will in most cases replace other cerebrovascular pathology although their reference is sometimes implied.

Due to the radiographic homogeneity of the tissues within the cranial vault, a simple radiograph will only reveal osseous structures as well as any radiopaque prostheses or tools. The use of radiography for brain imaging—and hence the birth of the field of interventional radiology—arose from the use of vascular imaging in diagnostic radiology as pioneered by the Portuguese radiologist Egaz Moniz who in 1927 published the use of what he called arterial encephalography, a method consisting of the injection of a contrast medium into arteries in order

to reveal the vessels anatomy with radiography [8]. This was necessary as the homogeneous nature of the tissues within the cranial vault made them invisible by simple X-ray roentgenography. A series of improvements by Engeset and colleagues permitted percutaneous access [9] later perfected by Seldinger [10], replacing Moniz's preferred surgical incision method, and whose technique is still employed today; contrast encephalography became highly successful and was rapidly adopted by radiologists worldwide [11]. The angiography, as it later came to be called, revolutionised the study of aneurysms and until recently was the only method available for the detection and study of intracranial vascular pathology, save for exploratory surgery or post-mortem necropsy [12]. Throughout the second half of the XX century numerous advances in imaging useful for interventional neuroradiology were developed. These included, among others, the digital subtraction angiography, CT angiography, MR angiography and the DynaCT angiography. The following section will attempt to provide a brief yet thorough overview of these important imaging modalities with respect to intracranial endovascular surgery, particularly, as previously mentioned, to the diagnosis and treatment of cerebral aneurysms.

Imaging Modalities

Plain film radiography

The scientific discoveries in radiation and particle physics during the Second World War and Cold War, led to exploration into medical applications of that technology. Hence, the field of medical radiology, or medical imaging, advanced in giant leaps during the latter half of the twentieth century. The following section will describe some of the most widely used imaging modalities in interventional neuroradiology and emphasis will be made on those that are of particular use for the preoperative study of vascular brain pathology and treatment planning and simulation.

The first Röntograms were live visualisations using a fluoroscopic screen. Eventually, techniques developed for photography were applied to radiography and silver nitrate films were used in order to preserve the images for later review. Although plain film radiography is arguably the most widely used imaging modality, it is not particularly useful in interventional neuroradiography as it provides scant temporal information and a simple two-dimensional view [11]. It must also be mentioned that fluoroscopy was also being used in order to perform live imaging of the body, however, due to the risk of radiation exposure by the operator and the relatively long exposure times associated with fluoroscopy rather than plain film radiography the use of this technique began to decline. Nevertheless, the use of digital planar-detector C-arm image intensifiers in modern angiography rooms means that live fluoroscopic viewing can be performed and selected frames can be saved. In addition, rotation of the arm allows for multiple views to be taken, and, if the subject's cranium is fixed, extrapolation can be performed to determine and volumetrically reconstruct the anatomy [13]. Moreover, the use contrast media during planar fluoroscopy permits time-lapse visualisation of blood flow, including flow patterns important in treatment planning such as vorticity, residence time of the contrast medium, etc. The most widely used contrast media for X-ray based angiography are iodine based although others do exist [14]. In fact, despite the advent of other more advanced imaging modalities, planar angiography still remains the gold-standard modality for the diagnosis of cerebrovascular pathology such as cerebral aneurysms [15]. Angiography, however is a relatively invasive procedure as it requires insertion of a catheter into an artery proximal to the vasculature of interest, or the catheter is inserted in a central artery and advanced just proximal to the region to be studied. Peripheral venous injection of the contrast is not particularly useful as significant dilution occurs precluding the adequate visualisation of the arterial vasculature [16].

Conventional Tomography

The technique known as conventional tomography—not to be confused with computed tomography, which is typically abbreviated CT—is mentioned here mainly for historical purposes. This modality involves the rotation of the X-ray source and movement of the film about the anatomy of interest keeping the structure in the focal plane. In actuality, this process is scarcely used as CT scanning can provide better resolution images; nonetheless, the principals involved in conventional tomography helped shape the dynamic CT scan (later discussed).

Computed Tomography (CT)

Computed tomography or CT is based on the principal developed by Sir Geoffrey Hounsfield, the 1979 Nobel laureate in Physics, that by processing data obtained from measurements of X-rays transmitted through a body in a circumferential manner, a tomographic—or slice—reconstruction of the body can be generated [17]. The first generation scanners were slow and resolution left much to be desired, however over the past few decades scanner technology has improved significantly. With the incorporation of multiple X-ray sources and detectors found in fourth-generation scanners, the spatial resolution has been dramatically increased as well as the temporal resolution with the use of rapid scanning by means of rapid-sequence helicoidal paths. With the development of CT scanning, visualising the brain became possible particularly due to the digital nature of the images produced which can be manipulated and processed to enhance certain tissues or features by use of intensity and contrast ‘windows’ based on the relative absorbance of radiation or attenuation of each tissue known as Houndsfield units. Again, due to the similar attenuation of vascular blood and surrounding cerebral tissue, standard CT protocols do not permit visualisation of the vessels, hence iodinated contrast agents are peripherally injected intravenously to increase the attenuation of blood revealing the vessel in what is known

as a CT angiography or CTA, which will be described in further detail later. In addition, digital subtraction is also possible with CTA, however the radiation dosage is doubled and hence is not widely used.

Magnetic Resonance Imaging (MRI)

Although CT scanning was one of the most important inventions in medical imaging and revolutionised imaging in neurology, unfortunately, due to the use of X-rays by CT scanners, a form of ionising radiation which in high doses causes tissue damage and has oncogenic effects at low and repeated doses, its use must be kept to a minimum. In addition, although CT scanning provides high resolution images of osseous structures and of the interface between tissues and liquid or air, CT provides poor resolution of tissues that are contiguous and have similar properties such as density. Nuclear magnetic resonance imaging, known commonly as MRI, on the other hand, works by capturing the different relaxation times of tissues after being subjected to a radio-frequency pulse under a strong magnetic field, a property that varies according to the relaxation properties of the hydrogen atoms—or protons— contained in different tissues. Due to the nature of MRI, tissues containing different molecular components can be accurately distinguished despite having similar densities. Moreover, MRI technology does not expose the patient or operator to the harmful effects of ionising radiation found in X-ray based modalities. In addition, MRI is able to detect flow phenomena, which will be of paramount importance for the discussion of MRI angiography [18]. Finally, MRI has the potential of serving as an alternative for intervention guidance instead of fluoroscopy, although the high cost and complexity of MRI scanners limits its use for this purpose at present [8].

Angiography

The use and importance of angiography has already been described briefly. The use of various contrast media injected into the arterial tree of the brain allowed for the visualisation of the vasculature in the brain enabling not only a method of diagnosis of cerebrovascular pathology and tumours, but also paved the way for the development of endovascular neurosurgery and remains the gold-standard for the diagnosis and planning of intervention for cerebral aneurysms [15]. Various types of contrast media have been used however, currently iodinated agents are the most widely used [19]. General convention has now opted for the term of invasive angiography to those procedures that involve and require gaining access to the vasculature in order to insert contrast into the vessel and perform imaging. However, direct angiography can be carried out by simply injecting the contrast into an artery as is commonly done with carotid angiography, or via a catheter inserted into a more distal artery which is advanced to the vascular tree to be imaged where the contrast is injected [20].

Angiography can also be classified as a diagnostic or an interventional procedure. In the former, the principal purpose of imaging is to obtain data for the purposes of determining the presence of pathology, the nature of the same and for any additional studies *ex vivo* before actual intervention. Conversely, interventional radiography implies that the main purpose of imaging is to guide a procedure, normally to treat or correct pathology or to obtain samples. Diagnostic imaging normally involves the acquisition of images or image sequences and storing them for further evaluation, whilst interventional angiography is employed to guide endovascular procedures. It must be mentioned however, that there is a fine line between diagnostic and interventional angiography and in many cases a diagnostic angiography is performed with intention to treat in order to avoid the necessity of two separate procedures and their inherent

risks. As previously mentioned, in endovascular procedures, angiography is performed using two C-arm detectors in order to have simultaneous views of the anatomy (see Figure 1.1) [13].

Since the images are digital, processing can be applied immediately after image acquisition. An example is a digital subtraction angiography (DSA), which is performed with a set of identical images save for one being taken without contrast, the mask, and another with contrast injection where the mask image is subtracted from the angiography as seen in Figure 1.2. As the only difference between both images is the contrast, then the contrast is the result of the mathematical operation permuting visualisation of the contrast inside the vessels, and hence the arterial tree, without it being occluded by the cranium and other radio-opaque features.

Angiography, particularly for intervention, is usually carried out with fluoroscopy. Originally, a fluoroscope was used in order to visualise both the endovascular instruments and the stream of contrast medium inside the vessels, however, today, this has been replaced by the use of flat-panel detectors and digital screens where the fluoroscopic angiography images are displayed in two-dimensions for easy visualisation by the operator [21]. A technological addition to live

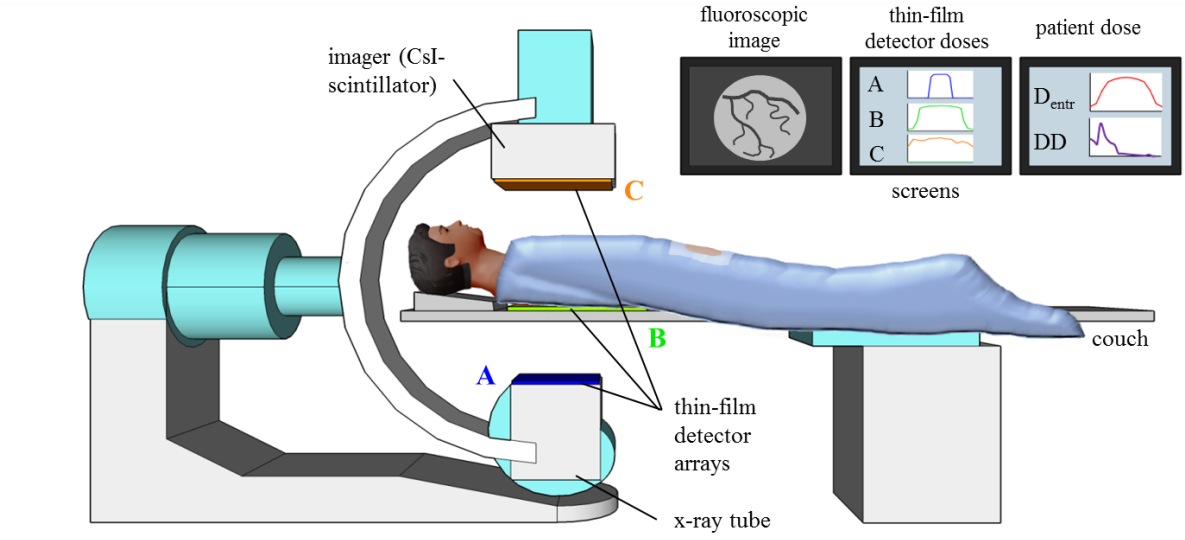


Figure 1.1: Typical C-arm fluoroscopy unit found in angiography rooms used for endovascular treatment. Image reproduced from Goertz and Zygmanski 2015 [13] published under an open licence.

angiography is the method of digital subtraction (DSA). This technique is particularly useful in interventional procedures: it involves obtaining an image of the angioarchitecture after contrast agent injection and then subtracting all other features in the image excepting the high-contrast vascular tree image obtained from the contrast angiography [22], [23]. The usefulness of DSA is indisputable as these images can later be saved as background phantom images and a real-time fluoroscopy image can be overlaid creating a modality known as "road-map" that permits the vascular surgeon to localise and advance a catheter through the vessels aided by a virtual vascular map without the need of further contrast infusions [23] [24]. More recently, the use of a 3D DSA has been used and is fast becoming the modality of choice for imaging in interventional neuroradiology as it permits the operator to see the relative position of vessels that would normally be overlapping in 2D DSA [22] [25].

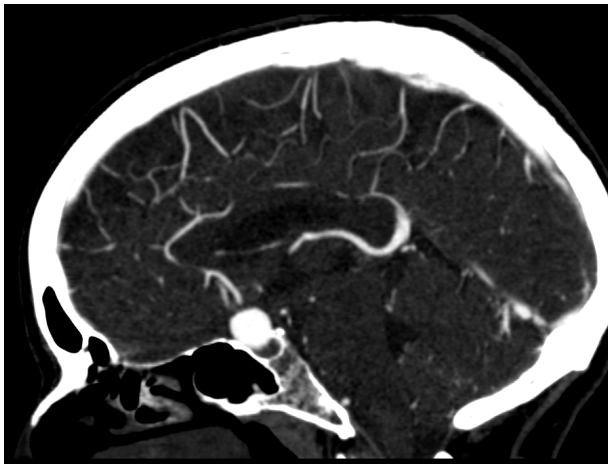


Figure 1.2: Example sagittal slice of a typical CTA study.

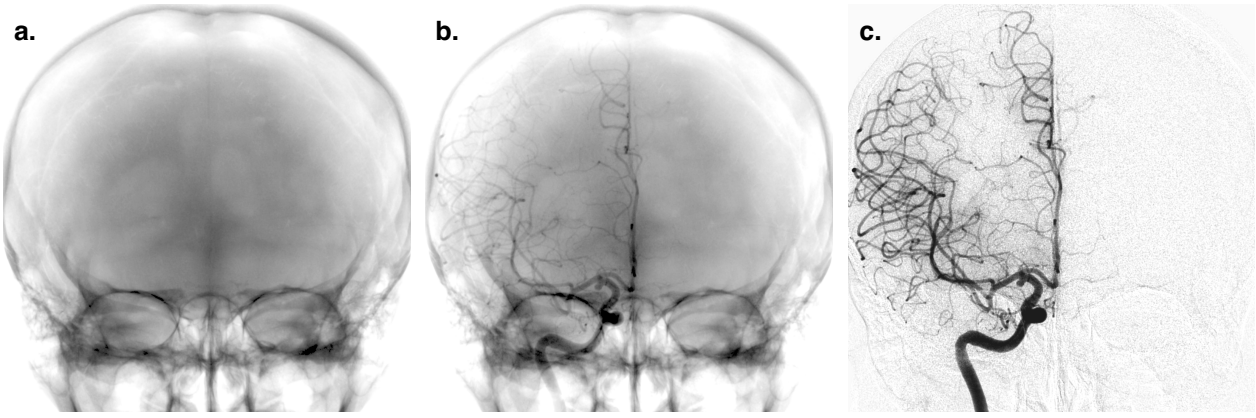


Figure 1.3: Angiography study with digital subtraction. (a) shows a planar X-ray without contrast, (b) during contrast injection, and (c) a digital subtraction image showing only the contrast inside the vessels.

CT Angiography

The use of CT imaging has already been summarised, however, the combination of angiography with computed tomography permits a better understanding of vascular architecture and allows for better preoperative planning. In reality no additional technology is required in order to obtain CT angiographs, however, due to its purely diagnostic nature, these scans are non-invasive and contrast media are injected into distal peripheral arteries. Consequently, this requires that the contrast injection be precisely timed in order to obtain an adequate perfusion of contrast in the desired vasculature during the image acquisition by the CT scanner. The images obtained can be manipulated in much the same way as CT images and certain tissues can be removed in order to reveal the anatomy of the vessels of interest. However, as will be explained later, the use of CT angiography has nevertheless been vastly replaced by dynaCT for reasons of convenience. Moreover, CT angiography has also been used for the generation of plastic models of vessels for preoperative planning and in vitro flow dynamics modelling [26].

Magnetic Resonance Angiography (MRA)

As was previously discussed, in addition to its high spatial resolution of soft tissues in particular, MRI is able to determine flow information by three different techniques, namely contrast-enhanced (CE) magnetic resonance angiography or MRA, and flow-enhancement methods including time-of-flight (TOF) MRA and phase-contrast (MRA). This is of particular interest for blood flow and haemodynamic determinations for the

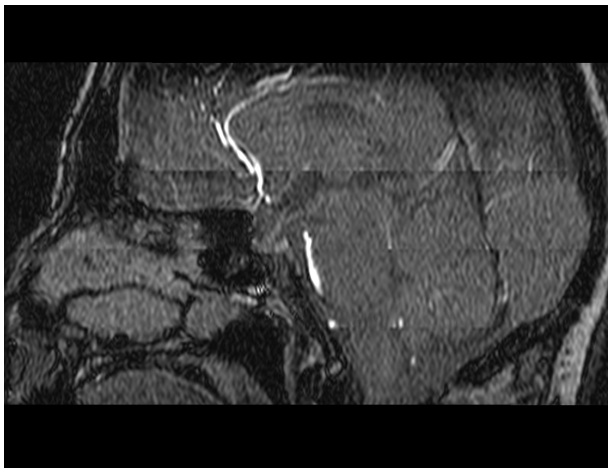


Figure 1.4: Example sagittal slice of a typical CE-MRA study.

intracranial vascular tree. CE-MRA, employs gadolinium, a paramagnetic contrast agent, and relies on the high T1 relaxation of this substance to enhance the visualisation of blood [27]. It provides adequate spatial resolution as well as a high signal-to-noise ratio (SNR) in comparison to flow-enhancement MRA. Like CTA, CE-MRA requires adequate synchronisation between contrast injection and image acquisition in order to ensure that the right vasculature contains the contrast. The use of gadolinium is however proscribed in certain medical conditions including renal insufficiency. TOF-MRA reveals blood by relying on slower exposure time, and hence lower saturation of flowing blood as it enters the area being imaged in comparison to stationary tissues that are exposed to the radio-frequency pulses. Therefore, TOF-MRA is able to map the magnitude of the flowing blood's velocity creating an image of the vasculature. A disadvantage of TOF-MRA is that it tends to reduce the caliber of blood vessels being imaged as in laminar flow the flow near the wall is much slower and therefore will appear darker and confused with stationary tissue instead of blood; this is particularly problematic with cerebrovascular pathology associated with slow flow or stationary blood such as in the case of cerebral aneurysms. PC-MRA uses a magnetic field gradient to introduce phase shifts to moving protons. In addition to providing the magnitude image of the blood flow, PC-MRA is able to determine the direction and hence provides full information on the velocity by providing a phase map [28]. This preceding point is of paramount importance for the generation of flow mapping in patient-specific 3D models of neurovascular haemodynamics and related fluid dynamics studies [29]. Nevertheless, a disadvantage of PC-MRA is that it is not able to cope with accelerating flow patterns and is therefore less useful with pulsatile and other non-uniform flow patterns. In order to obtain 3D MRA images, post-processing of the image must be performed. This is carried out by the

maximum intensity projection algorithm (MIP) which compares slice pixels to one another in order to reconstruct a 3D rendering of the vascular anatomy [30].

A more recent and highly useful method involves using a single C-arm to acquire a series of planar images as it rotates 180º around the cranium. This set of images are useful as they permit a volumetric visualisation of the cranium and of the vascular tree when contrast is injected simultaneously during acquisition. This method is commonly known as a rotational planar angiography. Furthermore, using computerised methods which will be briefly discussed below under computerised tomography, the raw data acquired in rotation angiography can be converted into tomographic axial slices including the use of a rotational sweep without contrast for digital subtraction. This method, commonly known as three-dimensional digital subtraction angiography or 3D-DSA, is particularly useful for visualising the architecture of the cerebral vasculature in isolation.

3D Rotational Angiography

Probably the most welcome advance in imaging modalities for use in interventional neuroradiology is the 3D rotational angiography, also known as the dynamic CT scan or dynaCT. Interventional procedures are not free of risks and when complications do occur it is necessary to obtain precise imaging in order to diagnose the problem. Traditionally, the patient would be taken to the CT suite in order to be scanned for problems. This not only poses risks inherent of interrupting an endovascular procedure but also, once the problem has been diagnosed, it delays the administration of the appropriate therapy which in most cases involves proceeding with the endovascular intervention [31]. Dynamic CT uses the same apparatus employed for 2D fluoroscopy during interventional procedures, however, in this case, the flat-panel detector (FD) mounted C-arm is permitted to rotate around the patients cranium during contrast bolus infusion

whilst acquiring serial fluoroscopic images that are then used to construct a 3D image of the anatomy in question comparable to that which a conventional CT scanner can obtain without the need of such equipment [32] [33]. Also, digital subtraction can also be carried out on these images and a 3D image can be underlaid of live fluoroscopy images for more accurate guidance during an interventional procedure [22]. Diagnostically, 3D rotational angiography, particularly reconstructed images, rapidly gaining ground in becoming the new gold-standard for aneurysm detection and intervention planning [34] [35]. As will be discussed, 3D angiography is also one of the preferred methods for obtaining 3D renderings of cerebrovascular architecture for patient-specific model reconstruction for use in blood-flow dynamics simulations [36] [37] [38] [39].

Ultrasonography

When it comes to interventional neuroradiology, ultrasonography is vastly underrepresented. This is probably due to the fact bone is mostly impervious to ultrasound therefore it is nearly inconceivable to obtain ultrasound images of the soft tissues contained within the cranial vault [40], although use of transcranial Doppler-ultrasonography is reported in the medical imaging literature [41], [42]. Nevertheless, ultrasonography has found a suitable niche in endovascular surgery as it is becoming widely used for image guidance during vascular access thus reducing complications, particularly in high-risk vessels such as the carotid arteries [43] [44]. Furthermore, Doppler-ultrasonography has also been used in determining flow rates in particular for the construction of haemodynamic models [45]. In addition, the miniaturisation of ultrasound transducer offers the promise of developing endovascular probes that might one day replace the necessity of fluoroscopy for exploratory and interventional catheterisation [45] [46].

At present, only the use of imaging modalities has been expounded however, the remainder of this article shall focus on processing of images and segmentation in particular as well as a brief

mention of the use of three-dimensional modelling with and without the simulation of blood-flow dynamics and the valuable data that has emerged from this novel technique.

Post-Processing of Digital Images

Although volumetric images rendered from digital subtraction methods such as 3D-DSA and CTA as well as MRA provide great visualisation of the intracranial angioarchitecture the images contain noise. In order to filter the noise, most medical software uses thresholding and smoothing; nevertheless, the noise is in fact not removed but rather hidden from view. A binary surface reconstruction of the 3D-DSA data would therefore contain noise and imperfections and would be useless for such applications including three-dimensional printing of models or use in computer fluid dynamics (CFD) studies. Hence, substantial amounts of post-acquisition processing are required in order to provide clean and accurate representation of the cerebral arterial tree. Various software packages bundled with medical imaging hardware exist as well as third-party suites, and open-source software are available. Software suites such as ScanIP/FE (Simpleware Ltd.) are able to post-process and segment features from many types of medical images, however a draw back is that these software packages allow the user to select different technique and parameters and hence the results of segmentation are user and technique dependant in the author's so experience and hence add another variable to the equation. In medical research, the open-source software is more widely used as well as bespoke solutions created on programming platforms such as MatLab [47]. Segmentation is one of many types of post-processing involving the isolation of features in a digital image and is further discussed as it one of the most researched techniques in image processing and one of the most useful in terms of anatomical modelling.

Segmentation

The process by which a single feature or group of features is isolated from an image is known as segmentation. Image segmentation is defined by Pham, et al. as “the partitioning of an image into nonoverlapping, constituent regions that are homogeneous with respect to some characteristic such as intensity or texture” [95]. There are a variety of segmentation techniques and algorithms and even more image processing chains that involve segmentation. In essence, segmentation involves pattern recognition and classification of features in an image so as to determine the similarity between the different components that make a single feature and distinguish that feature from the components that form part of other features or the background. These components are usually pixels in two-dimensional images which contain a single intensity value. Similarly, a volumetric image divided in a three-dimensional grid composed of individual voxels, this can be represented as multiple layers of two-dimensional images, or a stack, with measurement data encoded to preserve the volume information.

Segmentation involves coherence or a logical relationship that makes a whole, and therefore implies that a set of logical rules be followed to assess whether a pixel or voxel corresponds or not to the feature. This set of rules are known as an algorithm and can be represented mathematically, and in consequence codified and executed as a programme to process the image and segment the intended features. In addition, this programme can be initiated given the source data and additional input parameters and allowed to run continuously without interruption until the desired output is achieved and terminated, or initiated with the given source data as well as certain parameters and at set points, the programme is paused to permit review of the output data by the user who can then add or change parameters to obtain the desired output. When the algorithm is allowed to run without interruptions, the programme is normally said to be

automatic; conversely, when the user interacts with the algorithm after initiation and before termination, this is said to be a semi-automatic programme. There are different levels of automaticity when an algorithm is semi-automatic, however, even at it's simplest form, with constant user input, an algorithm, by definition has always elements of autonomy.

Cerebrovascular Disease, Imaging and Segmentation

Cerebrovascular disease is a common public health problem, including ischaemic stroke, haemorrhagic stroke, aneurysms and arteriovenous malformations among the most common. Not only is it one of the leading causes of mortality in developed countries, it is also the principal cause of chronic disability [48]. The treatment of cerebral aneurysms, for example, necessitates the accurate diagnosis before surgery or intervention is planned in order to plan the course of treatment. As with all diseases a detailed history and an appropriate work-up is required, however of upmost importance is imaging of the pathology which will allow the clinician to determine the relative risk as well as decide the best therapy for each particular case.

In the study of cerebrovascular disorders imaging is usually obtained prior to any intervention by means of non-invasive scanning using modalities such as computed tomography angiograms (CTA) or nuclear magnetic resonance angiography (MRA), or immediately prior to intervention using angiography and any of its derivative modalities described above.

In many cases, visualisation of the pathology is difficult. Tomographic modalities such as CTA and MRA, as well as 3D-DSA, provide axial slices and rapid repetitive scanning rostral and caudal through the stack is necessary for the clinician to develop a mental reconstruction of the geometry. Planar modalities such as simple angiography provide profile images which are able to show only one viewpoint at a time and often features such as larger vessels obscure other features

in the same path of X-ray transmission. Hence, planar angiography requires multiple acquisitions from different perspectives. Rotational angiography provides relatively complete visualisation of the vasculature as a 180º view is rapidly acquired during contrast injection. Nevertheless, the clinician still needs to scan the series of angular views in order to mentally reconstruct the anatomy. In addition, when implants such as metal plates, aneurysm clips, stents or coils are present, these create more obstructions or even artefacts that make visualisation more difficult. Therefore, multiple post processing techniques have been developed to remove and isolate the features of interest. Digital subtraction, which has been briefly explained above is one such processing technique that occurs at the time of image acquisition. Thresholding, is a simple method of segmentation: it maintains the feature of interest according to image intensity whilst attenuating, by using a low- and/or high-pass filter, those features that distract. Although useful for visualisation, the desired feature data is not always accurately separated from that which isn't, in consequence additional segmentation is required. The following section will briefly review the state of the art in terms of segmentation algorithms and techniques with a strong emphasis on cerebrovascular imaging. For a more comprehensive review of segmentation techniques the reader is referred to the work of Kirbas and Quek [49] and Lesage, et al. [50] as well as the original articles referenced to in the following summary.

The importance of the modality employed and quality of the data set used to obtain segmented images cannot be stressed enough. Presence of artefacts, noise as well as the signal-to-noise ratio will influence the required amount of pre-processing required before segmentation is performed as well as the overall quality and fidelity of the segmented feature. In some cases, post-processing is performed after segmentation in order to compensate for the errors generated by the segmentation process [49].

Although many segmentation algorithms combine different methods or can overlap in their classification, the following taxonomy of segmentation methods will be used to simplify the discussion: model-based methods [48], feature-based methods [49], and extraction-based methods [50]. It must be noted however that this classification scheme has significant overlap as is evident when comparing the works of Kirbas and Quek [49] and Lesage, et al. [50].

Models are used to determine if an image indeed conforms to the *a priori* qualities of the feature of interest. This involves drafting of assumptions that distinguish features. The most widely used models include appearance models in which the known properties of the vessels—or indeed the contrast contained within them—under certain imaging techniques, for example radio-opacity in the case of X-ray based modalities. This can be as simple as defining a vessel as having a higher brightness than non-vessel tissue. Similarly, the background or noise can also be modelled and therefore filtered out as was shown by Wilson and Noble [51]. Also commonly used are geometric models in which the known specific shape characteristics of, for example, an artery or an aneurysm, is used to guide a model. Surface models use the vessels' tubularity [52], and centreline models use the vessels' curvature in the case of two-dimensional images [53]. *A contrario* models are interesting in that they do exactly the opposite: they use prior knowledge to define what is not a vessel [54]. In addition, models can be constructed incorporating a combination of the above and other models to form hybrid models. Ridge models for instance combine intensity and spatial models to define ridges in the image corresponding to vessel boundaries [55]. Other models detect anomalies or variations from the norm in the vessels model such as bifurcations, aneurysms, stenoses and calcifications [50].

Feature-based methods exploit prior knowledge from models to determine features of interest from the general background. One of the simplest techniques use the fact that vessels containing

a contrast agent—as well as in flow-enhancement modalities—appear brighter than the surrounding tissue. Thresholding and windowing methods take advantage of this fact, however they may not be able to distinguish as they work globally on the image stack or individual image slices. Using intensity maxima it is possible to find vessels by determining local intensity maxima and using them as seed points for other segmentation algorithms [56]. Segmentation on intracranial vessels in X-ray-based modalities using brightness settings poses a challenge owing to their apposition on osseous structures which display similar intensity. In order to resolve this problem, techniques exist that detect edges or curvatures in features rather than only brightness. These methods employ second-order derivative information and are also able to determine the vessel orientation [50], [52]. Other methods determine how circular a cross section of a vessel is and use optimal line detectors to find the edges [57]. Another method of finding the edges of the vessel in the cross-sectional plane is ray casting. This method involves casting rays from a point inside the vessel lumen toward in all directions along the plane and detect the wall of the vessel. This method is also useful in finding the centre point inside the lumen where the difference in distance of all rays from that point is minimal, thus the centre point is equidistant, or optimised, to all points on the wall [58]. Finally, detection of features such as bifurcation or vessel anomalies for example stenoses, aneurysm and calcifications, helps simplify the vessel detection and segmentation by excluding these features from the image

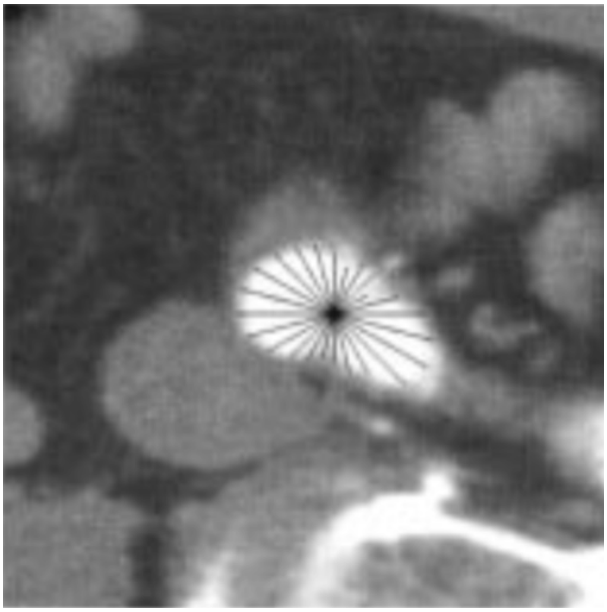


Figure 1.5: Example image of ray-casting technique (reproduced from Wink, et al. 2000).

once detected [50].

Extraction based approaches as named by Lesage [50] bare similarity to the schemes that Kirbas and Quek [49] called pattern recognition techniques. They employ assumptions based on models that describe the feature of interest, in this case the vasculature and use algorithms to detect patterns in the image that conform to the predefined patterns in the model. In a way, it could be said that in reality extraction-based methods integrate model- and feature-based approaches. They include some of the most widely used schemes including skeleton-based and region-growing methods. Extraction schemes require significant pre-processing to simplify the data and increase the accuracy of the segmentation. This can be as simple as cropping down the data to a smaller size, thresholding or applying filters to the data, resampling, etc., to reduce the total information needed to be processed as well as more complicated techniques which simplify the data without reducing its size by removing noise, artefacts, confounders, etc. In addition, pre-segmentation processes are required for the majority of segmentation schemes available. These include, for example, user-defined seed points or regions of interest, indicating the inlet/outlets of the vessels, taking measurements of the vessels' diameters, or defining the number of iterations or a critical value required by the algorithm. Some segmentation algorithms are able to determine many of these input parameters by themselves but this increases computational burden dramatically, introduces errors and in general drastically prolongs the time required to produce a segmented image.

Multi-scale approaches use varying resolution to extract features: large features are revealed at low resolution whilst small features at higher resolutions. This method is quite basic but is useful especially when combined with other methods as it simplifies the data for other extraction

techniques that require higher processing power [59]. The resolution may apply directly to the image or on a transform of the image in order to determine wavelets for frequency [60].

Region-growing schemes are one of the most popular segmentation algorithms. They work by iteratively adding neighbouring pixels or voxels in an image to a new image if they meet certain inclusion criteria. A seed point—or many—is usually required for the algorithm to initiate; moreover, the criteria used for comparison between pixels is normally user defined. These inputs can be simple intensity thresholds [61]. Some algorithms employ comparisons between feature and background [62] whilst others use morphological operators to grow the region of interest [63]. A related method is that of wave propagation where the region grows by means of an expanding front using inclusion criteria [64]. Wave propagation techniques are in a way ordered region-growing and hence can be more efficient as growing takes place only in a defined direction and also avoid retesting voxels. A different approach is that of active contours, also known as deformable models, and hence can be considered a model-based approach. These techniques use parametric curves, commonly called snakes, that deform under internal (model driven) and external forces (image driven) to find the contours of the feature [65]. Centre-line extraction methods produce a skeleton of the vessel but do not, by themselves, extract the lumen or walls of the vessels. For this, an additional algorithm is used that detects the edges from the centreline point, such as a ray-casting

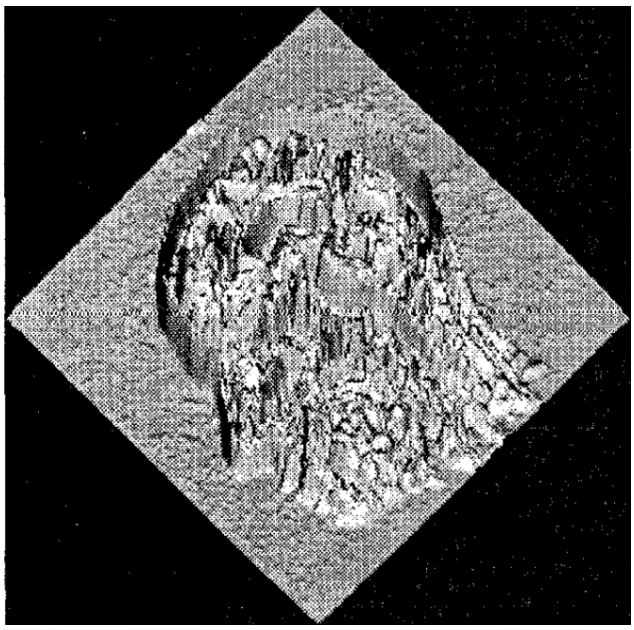


Figure 1.6: Elevation plot of an MRI slice showing ridges and crests (reproduced from Aylward, et al. 1996).

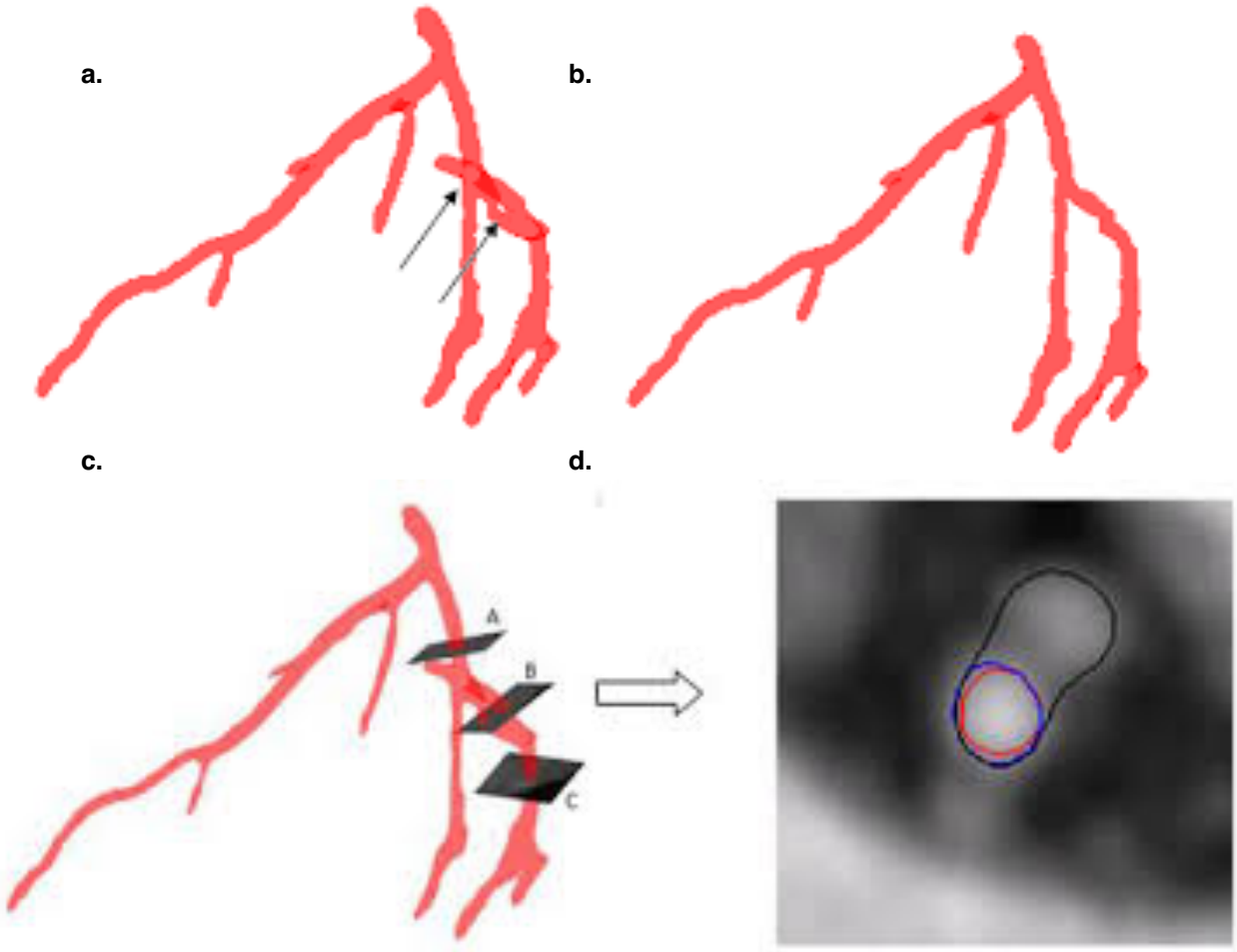


Figure 1.7: Kissing vessel artefacts. Image (a) shows an anomaly in the segmented geometry where vessels are erroneously connected, (b) shows actual anatomy, (c) and (d) show sections taken from the original image showing that the vessels in fact are separate (reproduced from Wang, et al. 2012).

technique (see Figure 1.5) [66] or cone-beam filtered back-propagation reconstruction [67]. In addition, centreline methods require seeding the inlets and outlets of the vessel tubes and usually only follow one path and thus require another seed in order to deal with bifurcations. They are however quite useful as vessel skeletons can serve as guides for interventional planning as well as for treatment simulations such as virtual stent deployment [68]. The minimal paths techniques also bears resemblance to centreline methods, however they are computationally intensive when performing segmentation on three-dimensional data [50] as are particle filters and related Bayesian techniques. By converting grayscale images into three-dimensional elevation plots (see Figure 1.6 from Aylward, et al. 1996), the resultant ridges can be used in order to determine the

centrelines of tubular objects by using watershed segmentation techniques; similarly the crests could indicate the edges of vessels for example [69], [70].

Lesage [50] further expands on post-segmentation techniques. These are remarkably important as they are necessary to ensure the accuracy of the final data produced after segmentation. Isolated vessels will very commonly have rough surfaces that need to be smoothed, or connections between adjacent vessels that don't in fact represent actual angioarchitecture, known commonly as kissing vessels [71]. In many cases, some vessels will be of higher caliber than in reality whilst others will be significantly thinned. Information may be missing altogether or non-vessel structures may be incorrectly incorporated. Hence many techniques have been developed that increase the accuracy of the final data set after it has been segmented. As previously mentioned, extracting centrelines for vessels creates a general map of the vessel tree. This tree can later be used to determine the vessel walls using techniques such as ray casting as previously described. The reverse process involves the extraction of the vessel wall anatomy and then skeletonising, that is extracting the centreline by progressively thinning the vessels, and then extracting the vessel tree. This vessel tree can be used to ensure that all vessels are present and eliminate kissing vessels which would not appear in the vessel tree but would appear as an anastomosis in the segmented angioarchitecture. Morphological operations on the image can correct errors, using dilation, erosion, closing and opening and recursive combinations of these basic techniques to achieve hole filling and smoothing for example. Discretising the image using finite element methods also helps post-process the image by applying smoothing algorithms to the refined surface or other finite element techniques. User input including measurement of, for example vessel diameters, can guide the post-segmentation processing to reduce the risk of vessel thinning or thickening.

Imaging & 3D Modelling

Many fields of medicine and surgery only require that a prompt diagnosis is made in order to treat and correct the problem as soon as possible. However, in interventional neuroradiology this is not quite the case: even the origins of this speciality were based on finding a suitable treatment option that involved a significantly reduced risk. In many cases before endovascular intervention was commonplace, many physicians chose not to operate intracranial vascular malformations or malignancies, as it was believed that the risk of complications would outweigh the benefit of surgery. Today, although endovascular intervention offers an option to the traditional treatment of these pathologies that included craniotomy, in the case of aneurysms, concern in the medical community has been on the rise. This anxiety is well founded as it is a well-known fact that not all aneurysms will be at risk of rupture during a person's otherwise natural life expectancy and the risk of morbidity and mortality from surgery may very well outweigh the risk related to rupture if untreated [72]. In addition, few aneurysms are discovered due to related symptomatology; some are incidentally found during other tests: routine or on account of another unrelated disease[32] [73] [74] [75]. Investigators from the International Study on Unruptured Intracranial Aneurysms published in 2003 a comprehensive multi-centric meta-analysis concerning the risk-benefit ratio of treating aneurysms and tentatively concluded "many factors are involved in management of patients with unruptured intracranial aneurysms. Site, size, and group specific risks of the natural history should be compared with site, size, and age-specific risks of repair for each patient" before a decision on course of treatment is taken [76]. However, this requires that a patient's probable natural history be extrapolated from statistics: a controversial mode of practice in a contemporary medicine that has been tending to move away from a patient-centred approach. What is more, each risk factor mentioned in the study only

contributes slightly to the risk of rupture-associated mortality in aneurysms. Other factors, not considered in the study might play a considerably more important role in defining the actual risk of rupture and of death consequently. The increasing accessibility to low risk imaging studies such as CTA and MRA has permitted that each individual patient receive adequate preoperative risk:benefit assessment; previously, this was done during exploratory angiography— with a significantly higher risk involved. Presently, the use of dynaCT and rapid 3D renderings of aneurysm angioarchitecture permit the interventionist a last-minute consideration on the decision to treat and of technique planning in case of the affirmative.

At the end of the twentieth century, biomedical engineers have attempted to study the influence of haemodynamics in the development, growth and ultimate rupture of intracranial aneurysms. Initially in vitro models, consisting of an ideal representation of cerebral vasculature were used [77]. Alternatively, in vitro models and simulations were performed on mould casts of dissected vessels from cadaveric specimens. These, however, are only useful for retrospective statistical analysis and are of little use when it comes to patient-specific therapy planning. Later, these models were built with the aid of 3D reconstructions from CTA images of living subjects. Owing to the difficulty and cost of building these models, during the past decade, interventionists have, with the aid of clinical engineers and medical physicists, been attempting to study the effects of blood-flow dynamics on computer-based simulations.

Previously, mathematical models were carried out on ideal structures simulation blood vessel morphology; however, these overtly simplistic simulations failed to provide information on a patient-to-patient approach. In 2003, Steinman, et al., published the first image-based computational fluid dynamics study using an aneurysm model from in vivo imaging of a living human patient [78]. The great surge in publications of this nature over the past years comes to

show how this emerging approach promises to focus clinical decision-making on a patient-centred basis rather than on statistical studies. Also, not only are the 3D-computational models now built from individual patient imaging, also haemodynamics are now being recreated from actual flow measurements using PC MRA or other similar methods, in order to accurately determine parameters that might play a role in the natural history of the aneurysm in the patient's particular case. These models have the potential of simulating how different therapies could alter and restore normal blood-flow dynamics that could lead to more efficient patient-based therapies. In order to accomplish the variety of steps required to perform CFD simulations, it is necessary to acquire medical images of high precision and rapidly segment the features of interest to be imported into the simulation software package. Segmentation has posed as a significant obstacle in this processing sequence due to poor accuracy of the resultant geometry or excessive processing time [79].

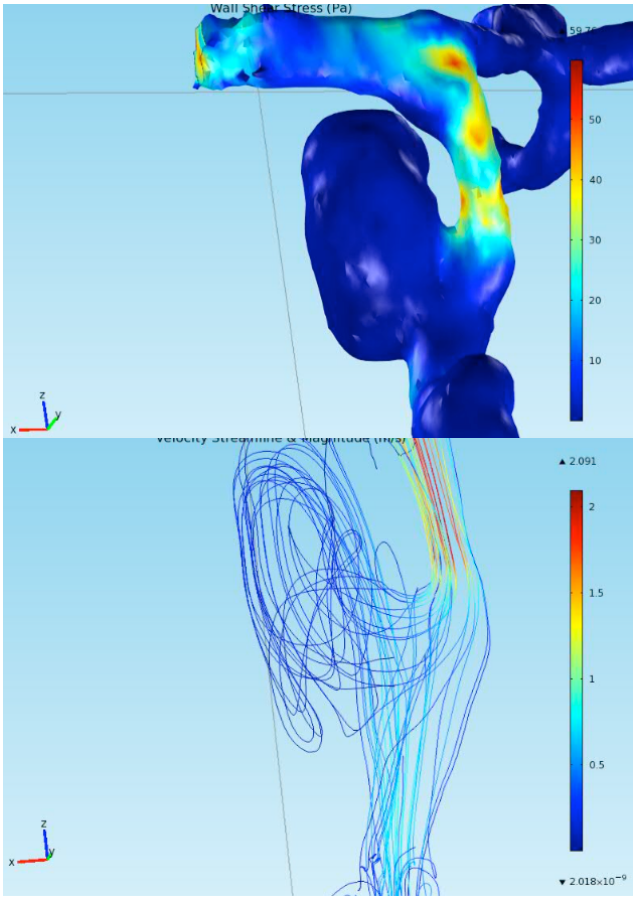


Figure 1.8: Example of a computer fluid dynamics study on a segmented artery and aneurysm (reproduced from Zajarias-Fainsod. 2010) [79].

In summary, many segmentation techniques and algorithms exist, with most being designed for specific data sets and for particular uses. The methods briefly mentioned above relate mainly to intracranial vasculature although many methods are used for thoracic and abdominal vessels,

as well as for retinal vessels, however retinal vessels employ two-dimensional techniques that in many cases serve as a starting point for three-dimensional algorithms. In the design of a new processing chain for extraction of the intracranial arterial tree, careful consideration must be taken on the appropriate image acquisition modality, the method and platform in which the images will be analysed, the necessary pre-segmentation processing techniques, quite obviously the segmentation algorithms employed, and their order of use if a combination is selected, and finally the post-segmentation processing required.

Moreover, although numerous image processing, segmentation and meshing software platforms exist, a notable example of which is ScanIP/ScanFE suite by the Simpleware Ltd., these platforms are not specifically tailored for one particular use and hence the techniques that they employ may not suit the imaging modality and intended use of the segmented volume. In addition the variety of settings and parameters that can be changed by the user apart from a selection of segmentation methods complicate replicability and add another element of variability and hence alter the result [79]-[81]. It is a well known problem, that choosing different segmentation thresholds, smoothing degrees, meshing type, etc. can alter the result of simulations that employ these volumes [82].

This thesis introduces a novel processing chain for the semi-automatic segmentation of brain vessels with an attempt at topology preservation for the accurate use in haemodynamic studies with emphasis on the segmented vessel geometry for use in computational fluid dynamics (CFD) studies. More techniques were considered, assessed, and tested than those that are discussed in the methodology described below, and only those that showed promise or led to advances in the selection process of the techniques used are exposed in detail. Moreover, a significant discussion

is presented detailing potential future research that might further improve the processing chain selected although this is beyond the scope of the current work.

Chapter 2: Data Selection and Pre-Segmentation Processing

Selection of Cases and Image Acquisition Modality

As previously discussed each medical image acquisition technique has advantages and disadvantages related to the principle by which each modality works. Those that use X-rays to obtain tomographic images of the skull and its contents are not able to elucidate the vessels and hence any pathology, therefore an iodine-based contrast medium is injected into the peripheral veins immediately before scanning. The major drawbacks to these modalities is the exposure to significant amounts of ionising radiation as well as the difficulty in differentiating contrast-filled vessels from osseous tissue or the blood—and hence contrast—containing meninges when these surround the vessels. On the other hand MRA provides images that clearly distinguish arteries from other tissues in the cranial vault. There is no exposure to harmful radiation and angiographies may be obtained by either using gadolinium as contrast agent or by using flow enhancement. Both CTA and MRA, being tomographic in nature, may be used to create 3D image stacks that may be used for processing or rendering of volume or surface images [83].

During endovascular treatment and in some selected cases planar angiography is used. It consists of capturing planar X-ray images of the brain from various angles and in some cases at time intervals. Contrast is injected directly into the parent arteries through a catheter placed proximal to the region of interest by obtaining central arterial catheterisation—an invasive procedure entailing a higher risk than peripheral infusion of contrast. By means of computer technology these images may have the skull and other radio-opaque features that obstruct the viewing of the arteries and its anomalies subtracted using digital subtraction as seen in DSA.

Considered the gold standard for treatment planning, DSA provides high quality images that permit precise measurement and location of aneurysms and are used throughout the intravascular treatment to guide the procedure. Rotational angiography obtains tomographic reconstructions and hence 3D renderings of the vessels alone by rotating the planar detectors by 180º once before and again while contrast is injected [84]. The first run is subtracted from the contrast run and a digitally subtracted 3D angiography (3D-RDSA) is obtained. Recently, 3D-RDSA has made sufficient headway and is rapidly replacing DSA as the gold standard used in treatment planning [36]. It must be clarified however, that protocols for imaging depend extensively on the individual centre and the resources at the disposal of the clinician.

The first process in the processing chain involves obtaining the medical image DICOM stack of brain vessel anatomy and converting it into a 3D logical array. Most cases were tested using 3D-RDSA owing to it being commonly found in most angiography rooms in high-level centres, is routinely performed and provides the most isolated images of the vessels from the background. Nevertheless, the algorithm was tested with CTA and MRA to determine its usefulness with these modalities. Data were selected retrospectively, obtained with consent for educational or research purposes, from patient cases belonging to Prof. James Byrne a senior interventional neuroradiologist at the John Radcliffe Hospital. Cases were chosen based on good imaging quality that allows a trained clinician to clearly distinguish features including normal, normal-variant and abnormal anatomy such as aneurysms. A total of five cases, three of which are abnormal in that an intracranial aneurysm is found in the vicinity of the circle of Willis and two considered to have normal/normal-variants anatomy were chosen for comparison of the segmentation technique with one abnormal case selected randomly to be used only for the purpose of illustrating the processing chain described in this work. The remaining cases bare

similarity in results but are not considered further. The image data was acquired using Siemens C-arm planar rotational radiography equipment using the 3D angiography modality.

Firstly the DICOM stack was imported and stored in the computer where processing will take place. The stack was saved in a directory as a multi-file stack with individual image files for each slice. Images were either 256 x 256 pixels or 512 x 512 pixels depending on the make and model of the C-arm detector and processor used in acquiring the images. Using MatLab a series of scripts were created (see Appendix A) and the directory was read using the available medical image package into a pre-allocated three-dimensional array with height and width equal to that of the pixels in the individual slices in the stack and depth equal to the number of slices contained in the stack. This information is contained inside the metadata alongside the DICOM file and can easily be read using the dicom.info command in MatLab. The value for each cell in the array may range from zero to 65,536 as standard DICOM images use a 16-bit grayscale. The typical stack height for a circle of Willis study is usually in the order of 100 slices resulting in an average of 25 million cells, resulting in a file size of over 400 Mb without compression. Once loaded, the image stack is displayed to the user by creating a video scanning through each slice. This allows the user to verify that the correct stack was loaded. Incorporating one of the available DICOM stack viewers or designing a graphic user interface displaying orthogonal slices will increase the usability of the segmentation programme in general.

Creation of Voxel Geometry

As previously mentioned, the data acquired from most imaging modalities is tomographic by nature, hence the stack of individual slices must be merged into a single data set before segmentation can take place. Each slice contains a grid of pixels, usually 256 by 256 or in higher

resolution images 512 by 512. In a way the individual slice images are two-dimensional matrices containing the grayscale value for each cell defining the pixel intensity. It is also important to mention that the grayscale values are most often 16-bit, that is to say they range from a lowest intensity of 0 represented by black to the highest $2^{16} - 1$ represented by white; most non-medical grayscale images are usually 8-bit. Although most screens used to display these images don't have the ability to display this range — consumer displays only display up to 256 shades of grey and medical monitors up to 4096 shades of grey or 12-bit [85] — it is important to note that the computation that takes place in the software package will make use of the 16-bit data and truncating or compressing the images simply because they exceed the display's capacity will lead to drastic loss of data which can potentially seriously impact the accuracy and precision of the segmented volume.

When imported into the MatLab software the metadata contained in the DICOM image stacks defines the size of a new three-dimensional matrix. The size of the matrix is defined by the width and height in pixels of the slices for M and N respectively. The number of slices in the stack then corresponds to the third dimension, P, in the matrix. Also extracted from the metadata is the pixel spacing which defines the width and length of each individual pixel, which will correspond to the base of the voxel, and the slice thickness corresponding to the height of the voxel. A three-dimensional matrix of dimensions M by N by P is created and pre-allocated and thereafter the image intensity is read into each corresponding cell or voxel. In most cases the slice thickness (i.e., the height of the voxel) is greater than the pixel dimensions. Therefore the image dimensions are resampled to conform to the new 3D grid and the values for the voxels are assigned by taking the weighted arithmetic mean of the pixel contribution for each voxel.

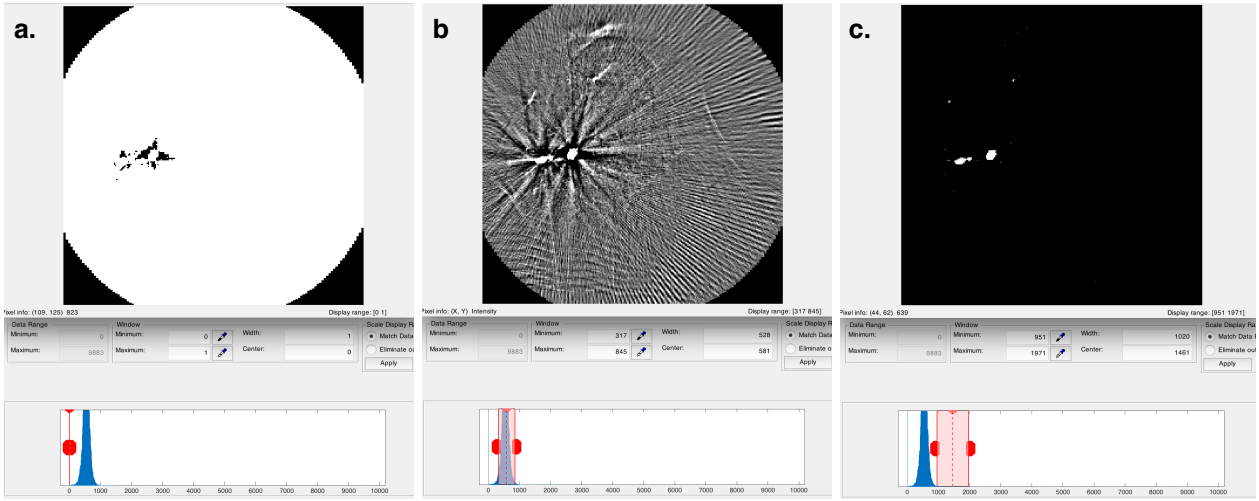


Figure 2.1: Brightness and contrast windowing and associated histograms for a sample slice of a DSA stack.

Windowing Enhancement

Although an effort has been under way to standardise the images obtained by different apparatuses of the same modality produced by a variety of manufacturers, in reality this is far from the norm [86]. In order to enhance features of interest in the images acquired, the viewer must alter the viewing parameters, including brightness and contrast, now made possible and highly dynamic by the use of digital acquisition and display. The process of windowing involves resetting the grayscale to include only the minimum and maximum pixel-intensity values contained in the feature of interest and adapting the scale. Although this can be done simply by only sampling and presenting these values in order to filter the image in preparation of segmentation it is necessary to actually eliminate below and above the values of interest and rewrite the images by selecting only intensity window values that contain the vessels and eliminating features and noise that have lower or higher intensity values. In most cases the user must define the values that provide optimal viewing but automation is possible. The procedure basically involves defining the minimum intensity value of interest and the maximum value of interest. Then all values below the minimum value are set to the minimum value, and all values

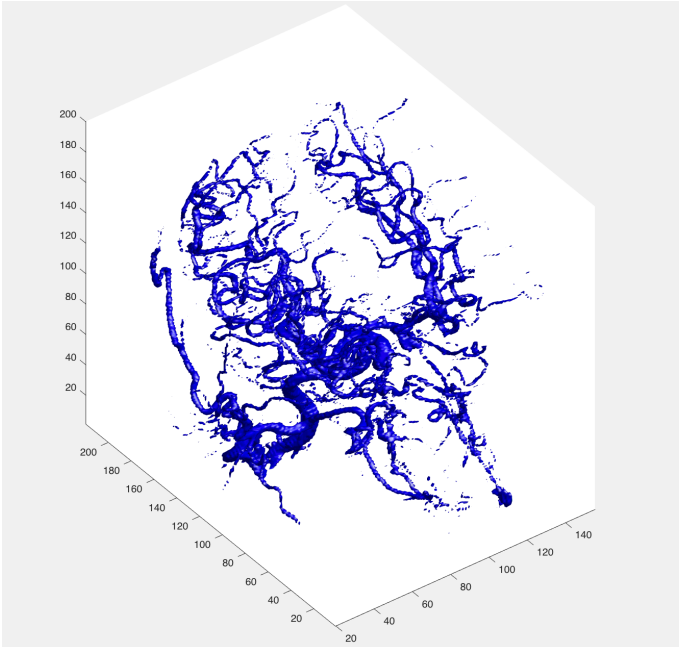


Figure 2.2: Surface rendering after thresholding DSA data set.

above the maximum value are set to the maximum value. The minimum value is then subtracted from all values and divided by the difference between the maximum and minimum to obtain a normalised scale (see Appendix A). Figure 2.1a shows the original data as imported with a normalised window, i.e., from 0 to 1, as can be seen from the histogram displayed below. Figure 2.1b shows a resampling of the data; note the high level of noise originating from contrast shadow artefact. Figure 2.1c displays the data after resampling the contrast range, eliminating noise and other background artefact. The peak in the histogram corresponds to the background. A surface rendering of the resulting thresholded data can be seen in Figure 2.2.

The main problem encountered with this approach is that as presented above, these thresholding values are global and an assumption is made that the average image intensity value of the contrast contained within the vessels is constant as the flow progresses through the cerebral arterial tree. This in fact is not true due to secondary flow patterns seen in tubular structures with high tortuousity and curvature [87]. Bifurcations, aneurysms, stenoses and other variations in the typical tubular structure of the vessels mean that the contrast will not be distributed homogeneously. Global thresholding methods usually result in either small vessel thinning and loss or large vessel thickening and incorporation of non-vessel features. Hence, a useful method

would be to apply a local adaptive thresholding value at each pixel based on a statistical analysis of image intensity in the surrounding area in order to ensure more accurate thresholding [88].

Cropping and File Size Reduction

Although most of the cells contained in the data stack are empty, segmentation algorithms work on the entire stack and must read the entire data set in order to process the images contained. In addition, the arterial tree in cerebrovascular images contain small branches that are not relevant. It is therefore appropriate to truncate the data by cropping the image. In order to facilitate viewing of the entire set an orthogonal projection (Figure 2.3) using the maximum intensity (MIP) created by the sum of the values of all the voxels along the normal of the plane in the projection. This is done by cropping in two dimensions on one orthogonal view (Figure 2.4a) and then again cropping the reduced set in another orthogonal view (Figure 2.4b). Once cropping is performed the resulting data is again

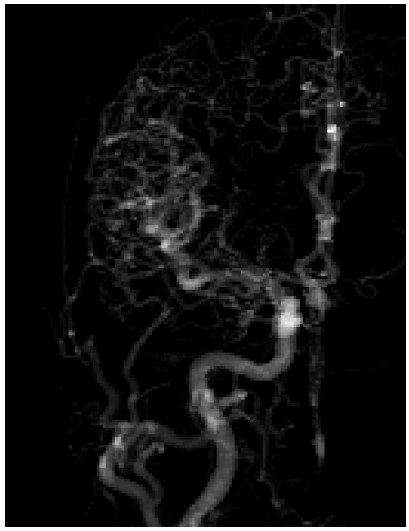


Figure 2.3: Maximum intensity projection on the coronal plane.

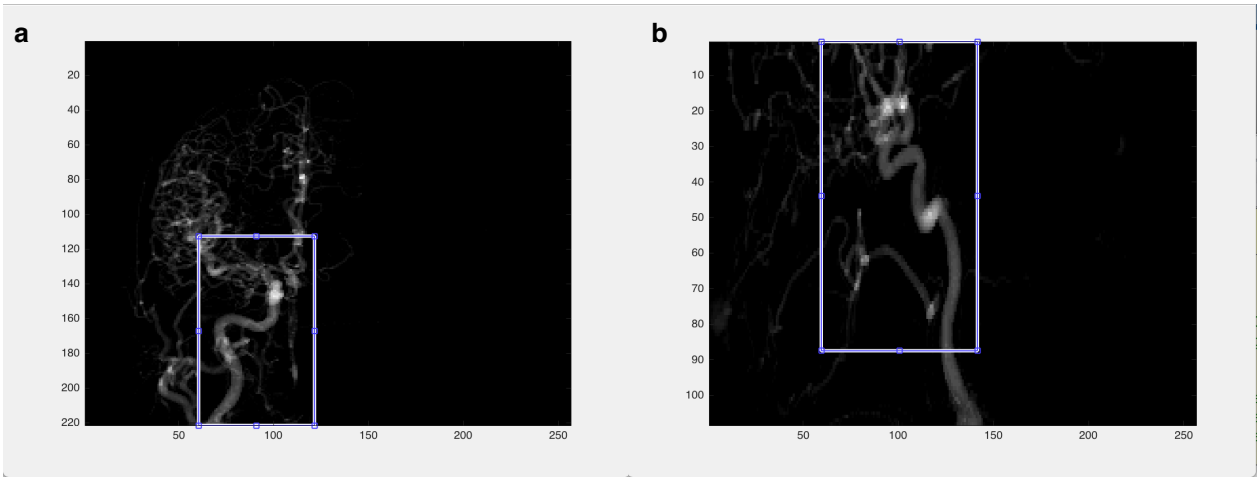


Figure 2.4: Simple graphical user interface created to show a maximal-intensity coronal projection (a) and sagittal projection (b) of the stack allowing cropping in both planes.

rendered using a surface plot. An example, using the same DSA data set is shown in Figure 2.5. Although the image is much simplified and the right internal carotid artery (ICA) is shown along its three segments, namely the osseous, cavernous and cerebral; as well as the main branches including the right ophthalmic artery projecting anteriorly from the cavernous section of the ICA, the remnants of a hypotrophied right posterior communicating artery (PcomA), the bifurcation of the right middle cerebral (MCA) and anterior cerebral arteries (ACA) and anterior communicating artery (AcomA) with a berry aneurysm at that location. Note the high quantity of vessel segments that are not continuous with the main vessels described above, examples of which are highlighted within red circles. Segmentation should adequately remove these discontinuous vessels and preserve all vessels originating from the seeded parent artery whilst avoiding the false anastomosis or 'kissing' of vessels in apposition.

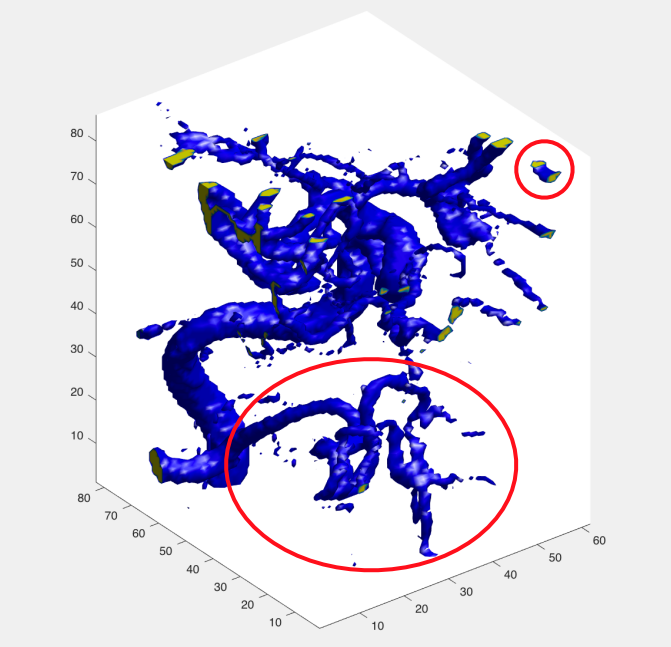


Figure 2.5: Post-cropping surface rendering of cerebral vessels from DSA. Note the large quantity of discontinuous vessels (red circles).

Chapter 3: Segmentation

Background

Image segmentation can be carried out by many methods as was discussed in the introduction. When it comes to angioarchitecture, differentiating continuity and apposition—i.e. the continuation of a single vessel versus the contact of two adjacent vessels—is of highest importance. Confounding apposition with continuity during segmentation leads to the creation of false anastomoses of vessels which when these geometries are employed in, for example, computer fluid dynamics simulations, a completely erroneous result will be produced as the input was flawed. Such is the nature of all models: their accuracy not only relies on the correctness of the model but also on the fidelity of the input data.

In the author's opinion, the most accurate way of determining pathological phenomena from imaging data is by careful observation by a trained clinical eye. Hence, it is logical to expect that the most accurate diagnoses are made by skilled radiologists. To date, the gold standard for diagnosing brain vasculature anomalies such as aneurysms and arteriovenous malformations is by manual interpretation of a CTA or other angiographic modality by a trained radiologist. For this reason, it was decided that automatic algorithms with or without artificial intelligence components should be excluded from this segmentation programme. The intention of this processing chain is to provide the clinician with a tool to extract the architecture and not to replace the clinician's diagnostic responsibility. Therefore, this processing chain involves input from the clinician in the form of locating the region of interest and cropping the stack in all dimension and lastly seeding the volume growing algorithm: the selection of the starting point or voxel in the volume of interest. In the example of a cerebral aneurysm, for which this software

has been optimised, using orthogonal cuts of the now voxelised geometry, the user, namely the interventionist, selects a point that is contained entirely within the aneurysm sac to act as a seed for the volume growing algorithm.

When a clinician observes an angiography study, they begin by locating one of the main arteries, such as the internal carotid arteries and the basilar or vertebral arteries, in one of the most caudal slices in the data set and tracking their progress through the stack rostrally. Using brightness typical of contrast or flow enhancement and the *a priori* knowledge about the tubular shape, the branching and thinning nature of arteries as they progress, the clinician is able to track the progression of the vessel and determine in each slice that which is artery, that which is not and the section of the artery visible as well as any pathology if present. When pathology is located, such as an aneurism, the radiologist starts by focusing on an area known to be part of the aneurysm and then proceeds to track the progression of the sac as well as to determine the neck and vessel from which the aneurysm originates. This method is akin to seeding in a segmentation algorithm. In other words, a point or voxel, known to belong to the feature of interest is selected and using feature or model-based schemes, the associated features are traced and 'grown' from regions already known to belong to the original feature. Hence, due to the similarity between a radiologist's methodology in analysing a medical image and region growing techniques, this extraction method was chosen as a basis for the processing chain designed in this work.

Since visualising three-dimensional images is of higher complexity than two-dimensional features, and designing a segmentation algorithm for two dimension is easier and can also be extrapolated to higher dimension—in this case only three dimensions were used although a fourth dimension can also be added, if the image is also a time-lapse image typical in cardiac chamber studies for example.

Two-dimensional image segmentation

In order to conceptualise the volumetric algorithm it was useful to first concentrate on a two-dimensional image. If a square grid with sides measuring *3x* is considered, subdivided into nine identical square cells with sides measuring *x*, the middle cell is taken to be the seed pixel. A circle is also placed concentric to the central square with a minimum radius *r* equal to half the diagonal of the smaller squares:

$$r = \frac{\sqrt{2}}{2}x$$

And a maximum allowable diameter *R* is equal to half the diagonal of the large square:

$$R = \frac{3\sqrt{2}}{2}x$$

Taking as an example a circle with a radius *r*, the points on the circle with centre at the origin are determined by:

$$r^2 = x^2+y^2$$

The central seed square pixel is entirely occupied by the area of the circle. The four neighbouring pixels sharing a side with the seed pixel, or side pixels, each contain an area given by the area under the curve between $-0.5 \geq x \geq 0.5$ minus the area of the seed pixel found above the *x*-axis, with origin at the centre of the circle, equal to one half of the area of one pixel or $0.5x^2$.

$$\int_{-0.5}^{0.5} \left(\sqrt{r^2-x^2} - \frac{x}{2}\right) dx$$

Similarly, the area of the circle occupied by any of the four neighbouring pixels that share a point with the seed voxel, or corner pixels, is given by the area under the curve between $0.5 \geq x \geq 1.5$ minus half the area just calculated in the equation above, or

$$\int_{0.5}^{1.5} \sqrt{r^2-x^2}\,dx - \frac{1}{2}\int_{-0.5}^{0.5} \left(\sqrt{r^2-x^2} - \frac{x}{2}\right)dx$$

Empirical analysis shows that the eye recognises a square of a grid as containing or being significantly occupied by a figure not when half the area is occupied but when the intersection of the edge of the figure is beyond the midpoint of the edges of the square in the grid (Figure 3.1). A simple experiment was conducted by showing five volunteers a series of sequential images as a MatLab movie like the one shown in Figure 3.1 with the size of the circle starting so that the circumference of the circle intersected with the corners of the central square. The size of the circle was progressively increased in sequential images and the volunteers were asked to stop the movie when they considered that a *significant area* of the neighbouring squares—first with the side and then the corner neighbours—was occupied by the circle. No statistical analysis was performed on the results due to the low sample number of participants but it was consistent among all participants that they had determined that the area was occupied by the circle when the circumference of the circle passed the midline of the squares. Further experiments are required to obtain statistical significance and proof of this

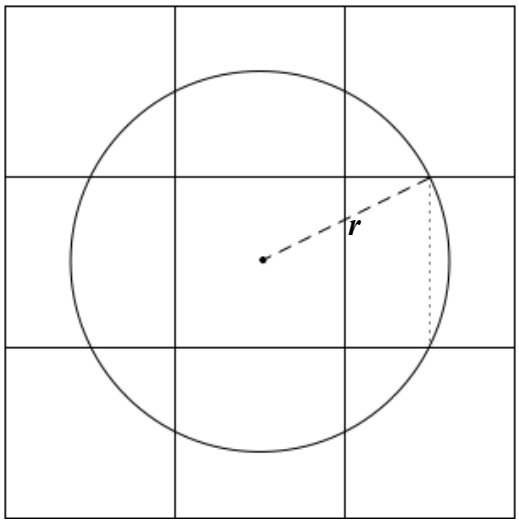


Figure 3.1: Determination of the radius of a circle when the midpoint of an edge-neighbour is intersected.

preliminary concept. Hence, for the edge-sharing or side pixels the radius of the circle must be greater than $\frac{\sqrt{5}}{2}x$, thus the total area of the side pixel occupied by the disk is equal to:

$$\int_{-0.5}^{0.5}\left(\sqrt{\tfrac{5}{4}-x^2}-\tfrac{x}{2}\right)dx$$

Dividing this area over the area of the square, or x^2, we obtain that the occupied area represents 58% of the area of the square. If we consider the seed pixel to have a maximum possible intensity value normalised to 1 and the background a minimum intensity value of 0, any neighbouring pixel having half its area occupied by the circle representing the area of interest will have a pixel intensity value of 0.5. A pixel having 58% of its area would therefore have an average pixel intensity of at least 0.58 and the difference between the reference pixel and the neighbouring pixel not be greater than 0.42 or 42%.

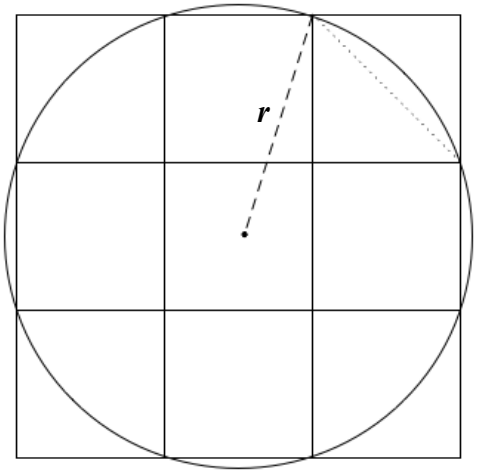


Figure 3.2: Determination of the radius of a circle when the midpoint of a corner-neighbour is intersected.

For it to be said that the corner pixels contain the image, the intersection of the edges must also lie beyond the halfway point in the square however in this case the square is aligned diagonally and hence this point is the vertex of the square that lies along the side of the grid (Figure 3.2). The distance to the centre, and the radius of the circle, is now equal to $\frac{\sqrt{10}}{2}x$, which results in a total area of the corner square occupied by the circle of:

$$\int_{0.5}^{1.5}\sqrt{\tfrac{5}{2}x-x^2}\,dx-\tfrac{1}{2}\int_{-0.5}^{0.5}\left(\sqrt{\tfrac{5}{2}x-x^2}-\tfrac{x}{2}\right)dx$$

Again, we can determine the percentage of the area of the corner square that is occupied to be 65.9% with an average pixel intensity of at least 0.659 and similarly the difference between the reference pixel and the neighbouring corner pixel not be greater than 0.341 or 34.1%.

In order to determine if a neighbouring pixel still contains the area of interest it is necessary to determine the difference or error in pixel intensities that is permissible before the neighbouring pixel is considered not to contain the area. It must be noted that this will only work with binary images or images where a look-up table is used to separate features into different images. The error (ε) in value for a neighbouring pixel is given by the value of the pixel being tested (v_t) and the original value of the reference pixel (v_r), which in the first iteration this is the seed pixel, or:

$$\varepsilon = |v_t - v_r| \,/\, v_r$$

Therefore the algorithm will test neighbouring pixels to a reference central pixel, which will take a normalised image and convert it into a binary segmented image where members belonging to the feature will be given a value of 1. If the reference pixel value's difference is less than the allowable error threshold then it will be incorporated into the segmented images area. In other words, the algorithm first assigns the new binary value of 1 to the seed pixel, it then compares the original value of the seed voxel with each neighbouring pixel. If the value is within the margin of error—for a side pixel 0.42 and for a corner pixel 0.341—then it belongs to the same feature and is given the new binary value of 1, otherwise, it is assigned the null binary value of 0. This is done using the following moving mask on the test image:

$$\varepsilon = \begin{bmatrix} 0.341 & 0.42 & 0.341 \\ 0.42 & 1 & 0.42 \\ 0.341 & 0.42 & 0.341 \end{bmatrix}$$

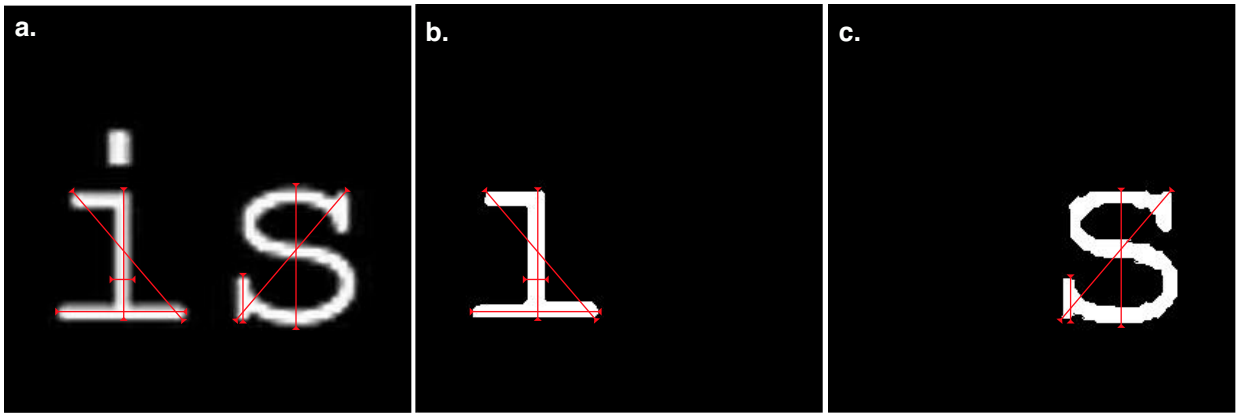


Figure 3.3: Test of the region-growing segmentation algorithm on a two-dimensional negative image: (a) original image containing two characters; (b) segmentation of the first character by seeding inside the character with the result excluding the dot; (c) segmentation of the second character by seeding inside the character. Red segments correspond to measurements taken for comparisons.

The step is reiterated for all pixels that were assigned values of 1 but using its original intensity value and comparing it with the remaining neighbours not included in the previous iteration. The algorithm continues iterating until the end of the geometry is reached or no further pixels are included by performing another iteration.

This segmentation method has the potential for high accuracy since the margins of error used depend on the local values of the image rather than the statistical distribution of the entire image which is usually—in digital subtraction in particular—empty or composed of noise more than valuable information. This is similar in a way to a locally adaptive method as described above for thresholding. In essence, this algorithm determines the probability that the mask grid lies on the edge and then if the probability is high it defines the edge by assigning pixels within the boundary as true and those beyond as false. Standard deviation methods are not, in the author's opinion adequate as this assumes that the distribution of intensities in the feature are Gaussian which is not the case once the background has been eliminated and since the contrast becomes inhomogeneous and more dilute further up the arterial tree, especially after windowing as outliers and extremes in the histogram have been cropped out previously.

In order to test the accuracy of the two-dimensional segmentation algorithm a test image was used. This image, composed of a negative grey-scale rendering of the text ‘is’ was used since the shapes of the letters have elements that are found in vascular imaging such as branching and discontinuity in the letter ‘i’ and tortuousity in the letter ’s’.

Running the region growing algorithm without the mask and using an arbitrary permissible error threshold value of 0.05 yields results that are clearly smaller in area than the original image to the naked eye. Conversely using a single threshold of 0.25 results in an overgrowth of the area in question. Applying the mask yields significantly better results; measurements taken of various parts of the original image (e.g. length, width of stem of letter) with its counterpart on the segment image as shown in Figure 3.3, and analysing the pairs of data using a non-parametric Wilcoxon matched-pairs signed rank test for continuous variables resulted in a P value of 0.2241 indicating that the measurements are not statistically different. The Wilcoxon test was chosen because of the paired, non-Gaussian distribution nature of the data and has been previously used in other statistical studies of aneurysm geometries [89]. The linear regression of the data (Figure 3.4) results in a slope of 0.9892 ± 0.005295 with an R^2 value of 0.9997. Identical data sets would have yielded a linear regression with a slope of $m = 1$ and $R^2 = 1$. Additionally, the sum of the ratio of the differences between the measurements in the original image and the segmented image

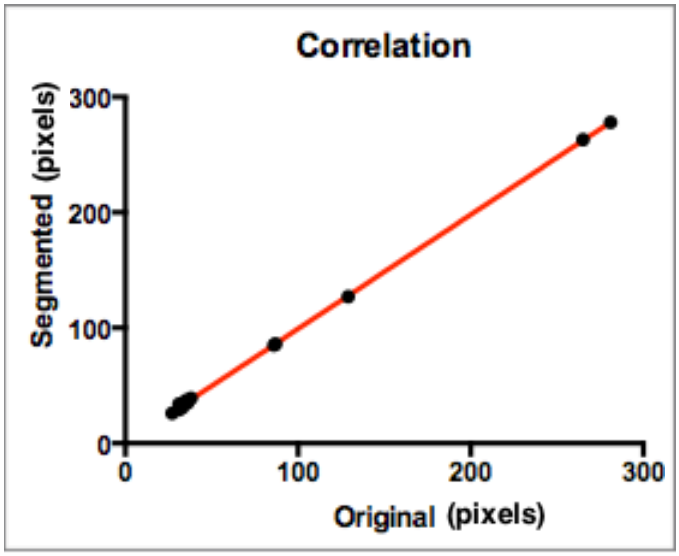


Figure 3.4: Linear regression of various paired measurements of length in pixels taken from the original image and the corresponding measurement in the segmented image as shown in Figure 3.3.

was 0.0027 or 0.27% which indicates a significantly high correlation between the paired measurements. Hence, it can be concluded that this segmentation algorithm results in negligible decimation or dilation of the segmented area.

Segmentation by volume growing algorithm

For a three-dimensional image discretised into voxels, the seed point, which in reality is a voxel, is surrounded by six voxels with which it shares a side, twelve voxels sharing an edge and a further eight voxels sharing a point (see Figure 3.5, the red cube is the seed voxel surrounded by its neighbouring voxels). Consider a large cube of sides *3x* composed of 27 identical smaller cubes with sides measuring *x*. Inside this cube is inscribed a sphere where the sphere represents a volume of interest and the seed cube has dimensions so that the entire volume of that cube is contained within the sphere (Figure 3.6). In addition, the large cube (composed of the 27 smaller cubes) must never be fully contained within the sphere, as this would result in repeating the first condition at a larger scale. Therefore the minimum radius *r* for the sphere (i.e., when the seed cube is fully inscribed inside the sphere and the diameter of said sphere is equal to the length of the diagonal of the small cube) is:

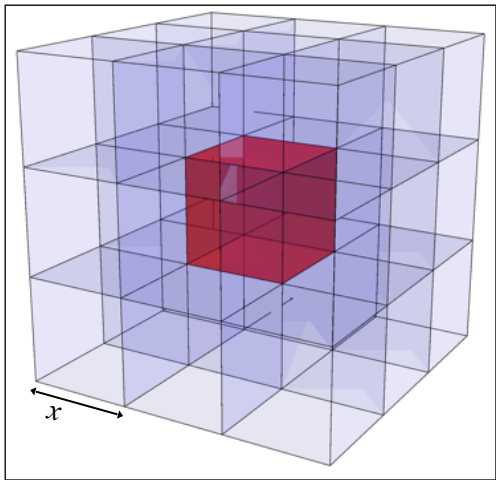


Figure 3.5: Representation of a seed voxel surrounded by all its neighbouring voxels.

$$r = \frac{\sqrt{3}}{2}x$$

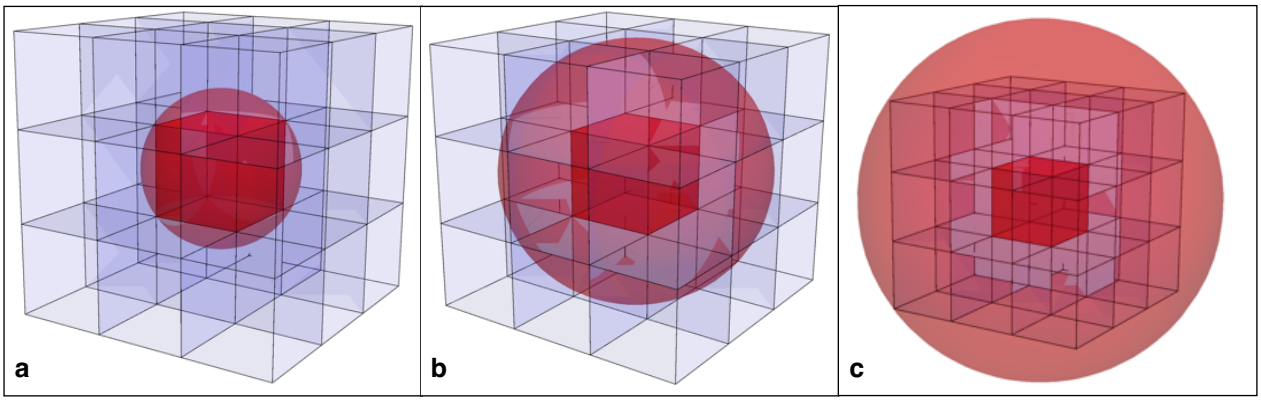


Figure 3.6: Representation of a spherical feature: (a) show the smaller possible size for the sphere still having the seed voxel fully inscribed, (b) the sphere fully inscribed within the entire set of cubes, and (c) the larges possible diameter of the sphere, analogous with the first case, indicating a problem of scale.

Alternatively the maximum possible radius R for the sphere is less than half the diagonal of the large cube or:

$$R = \frac{3\sqrt{3}}{2}x$$

Therefore the radius of the sphere is given by:

$$\frac{\sqrt{3}}{2}x \leq R < \frac{3\sqrt{3}}{2}x$$

The central small cube is taken to be the seed voxel and the sphere is the feature of interest (Fig. 3.5). The task is to determine what percentage of the volume of a cube must be occupied by the sphere to consider that the cube contains the part of the feature. When switching to imaging terminology, the previous can be rephrased as determining the maximum allowable difference in voxel intensity between the seed voxel and the neighbouring voxels. Again, the seed voxel is known to be fully contained within the volume of interest and the neighbouring voxels make up the volume of interest to a certain extent. For the simplified geometric example, the neighbouring cubes are all part of the edge of the sphere. In both instances the seed voxel is 100% inside the feature. The remainder of the feature however is shared by the other voxels in different

proportions. To simplify the calculation the case of the seed voxel being fully inscribed in the sphere will be used (Figure 3.6a). The voxels that share only one point with the seed voxel, or corner voxels, do not contain any of the volume of the feature, and hence are not considered. To each side, those voxels sharing one face with the seed voxel, or face voxels, contain a greater proportion of the remainder than those sharing an edge, or edge voxels. This proportion changes as the radius R of the sphere grows. The question is to determine at which percentage of occupancy of the volume of the cube by the sphere is the cube said to be part of the sphere as was done with the planar grid case. It is therefore reiterated that the inclusion of voxels as part of a feature of interest in a volume growing algorithm not be based on algorithms utilising normal distribution but rather on a neighbour-to-neighbour voxel basis. That is to say, if a voxel is known to contain a feature, the likelihood that the adjoining voxels also contain the feature is higher — obviously considering that face neighbours are more likely to contain the feature than edge neighbours and even more so than corner neighbours. Conversely, if a voxel does not contain a feature, the likelihood that the neighbouring voxels contain that feature is very low, as continuity is a prerequisite for volume growing. Therefore the volume occupancy percentages are used in calculating a weighted probability of a feature being shared by neighbouring voxels. In order to exemplify this algorithm, a simplified two-dimensional area-growing algorithm was explained earlier.

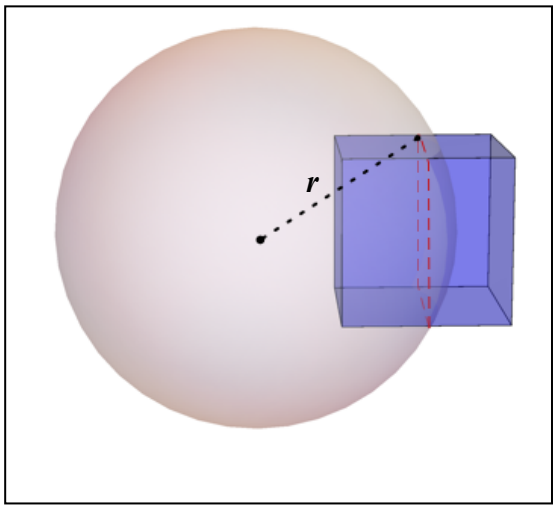


Figure 3.7: Determination of the sphere radius for majority occupancy of the side neighbour voxel.

Drawing parallels between the planar grid and the volumetric grid in the tree-dimensional image, we can consider a face neighbour to contain the sphere when the intersection of the sphere is at least beyond the midpoint of its edges (Figure 3.7). This occurs when the radius is equal to or greater than $\frac{\sqrt{6}}{2}x$. To calculate the volume of intersection of the sphere and the cube we similarly calculate the volume under the surface of the sphere inside the cube as was done for the area in the square above. Every point on the surface of the sphere is given by a function defined as *f(x,y,z)*. The value of *z* is in fact a function of *x* and *y* or *z=f(x,y)*. With a sphere centred at the origin, the radius *r* will be equal to the maximum value of *z* which coincides with the minimum values for both *x* and *y*, or *r=z(0,0)*. Hence, the volume for the central segment is given by the following double integral:

$$\int_{-0.5}^{0.5}\int_{-0.5}^{0.5} f(x,y)\,dx\,dy$$

Furthermore,

$$f(x,y)=\sqrt{r^2-x^2-y^2}$$

Which means the volume is determined by calculating the integral and removing the section of the seed voxel included in the integral above equal to half the volume of a cube or x^3:

$$\int_{-0.5}^{0.5}\int_{-0.5}^{0.5}\sqrt{r^2-x^2-y^2}\,dx\,dy \;-\; \frac{1}{2}$$

Note that the last term does not contain x^3 and is not meant to be integrated; in reality represents z^3, or better a shift in the *z*-axis in actual terms but was explained as x^3 as the cubes measure *x* in all dimensions. Substituting for $r=\frac{\sqrt{6}}{2}x$ and evaluating and dividing by the volume of the cube to obtain the proportion of the volume of the cube occupied by the sphere yields

approximately $0.654x^3$ or 65.4%. This indicates that the threshold difference between the intensity value and any of the six voxels sharing a face with the seed or reference voxel, and the seed or reference voxel should not exceed 0.346.

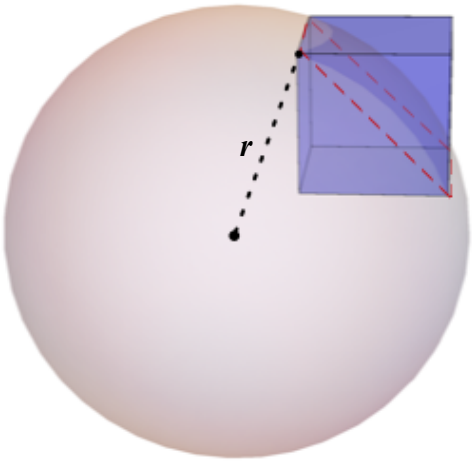


Figure 3.8: Determination of the sphere radius for majority occupancy of the edge neighbour voxel.

For an edge neighbour the same calculation is carried out with a radius of $\frac{\sqrt{11}}{2}x$ and modifying the integration limits to coincide with the section of the three-dimensional grid for an edge neighbour (Figure 3.8). However since the radius now is more than $1.5x$ then the volume of the sphere will be partly outside of the cubic grid and when integrating this must be taken into consideration to avoid adding this volume. It must be noted that at this radius size the edge neighbour can be integrated simply between x=0.5 and x=1.5 and y=-0.5 and y=0.5. Had the radius been smaller then the integration bounds for x would have been between x=0.5 and $x=\sqrt{\left(\frac{\sqrt{11}}{2}\right)^2-\frac{1}{4}-y^2}$. Nevertheless, as the radius is in fact larger and the sphere is partly outside the dimensions of the grid, this means that a small volume of sphere has to be subtracted. This can be done by using the above mentioned integration bounds for x and only integrating for $z \geq 1.5x$ by solving the following equation for the volume contained in an edge neighbour:

$$\int_{-0.5}^{0.5}\int_{0.5}^{1.5}\sqrt{r^2-x^2-y^2}\,dx\,dy \;-\frac{1}{2}-\int_{-0.5}^{0.5}\int_{0.5}^{\sqrt{r^2-\frac{1}{4}-y^2}}\sqrt{r^2-x^2-y^2}\,dx\,dy \;-\frac{3}{2}$$

Thus we obtain an occupied ratio of $0.728x^3$ or 72.8% which defines the segmentation threshold of pixel intensity difference of less than 0.272.

Finally, we calculate the volume occupied by the sphere in the case of the corner neighbour (Figure 3.9). This is done similarly and a radius of $r = \frac{\sqrt{19}}{2}x$ is used in order to consider the cube as significantly containing the sphere. In order to calculate the volume we must again first find the volume under the surface of the sphere above $z=1.5x$ and then subtract the volume of the sphere within the bounds of integration—now between $x=0.5$ and $x=1.5$ and $y=0.5$ and $y=1.5$— but beyond the grid. In like manner as for the edge neighbour the equation used is:

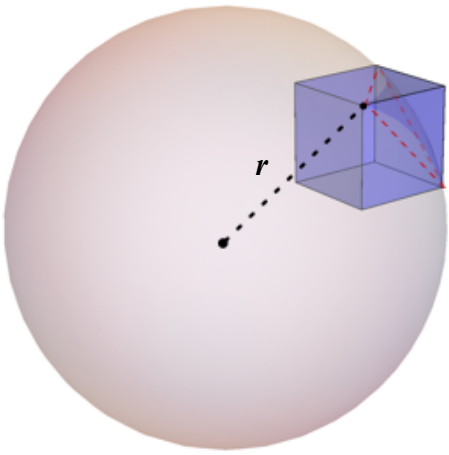


Figure 3.9: Determination of the sphere radius for majority occupancy of the corner neighbour voxel.

$$\int_{0.5}^{1.5}\int_{0.5}^{1.5}\sqrt{r^2-x^2-y^2}\,dx\,dy \;-\; \frac{1}{2} \;-\; \int_{0.5}^{1.5}\int_{0.5}^{\sqrt{r^2-\frac{1}{4}-y^2}}\sqrt{r^2-x^2-y^2}\,dx\,dy \;-\; \frac{3}{2}$$

Solving for a sphere with a radius as mentioned yields an occupied volume of $0.924x^3$ or 92.4% of the volume of the cube. As a consequence, the error threshold used for the corner voxel will be 0.076.

It is important to not that the thresholds for the face, edge and corner voxels are different and are progressively smaller at 0.346, 0.272, 0.076 respectively. Thus, the following moving mask is applied to the image:

$$\varepsilon = \begin{bmatrix} 0.076 & 0.272 & 0.076 \\ 0.272 & 0.346 & 0.272 \\ 0.076 & 0.272 & 0.076 \end{bmatrix}; \begin{bmatrix} 0.272 & 0.346 & 0.272 \\ 0.346 & 1 & 0.346 \\ 0.272 & 0.346 & 0.272 \end{bmatrix}; \begin{bmatrix} 0.076 & 0.272 & 0.076 \\ 0.272 & 0.346 & 0.272 \\ 0.076 & 0.272 & 0.076 \end{bmatrix}$$

In addition, since the volume-growing algorithm is recursive, an edge voxel that has been included will then become the reference voxel in a later iteration. Therefore, if a corner voxel was excluded in an initial iteration, it might be included at a later stage when it becomes the edge voxel of a new reference voxel which was previously a face voxel in turn, or even later as the face voxel of an edge voxel now taken as a reference voxel in this new iteration.

Segmentation by volume growing algorithm

Once the algorithm was designed and the necessary parameters defined as explained in the previous section, the algorithm was implemented in MatLab. In order to facilitate the interaction with the user and in addition simplify debugging, some graphical user interfaces were incorporated. The script Orthogonalslicer created in 2009 by Lazlo Balkay of the University of Debrecen, was incorporated as the first step and is used to load the cropped image stack and display three orthogonal slices simultaneously which permit interaction between the views (Figure 3.10). In addition, choosing an adequate seed point, for example inside an aneurysm, is simplified. Once the coordinates for the seed point are chosen the user inputs them into the next screen starting the segmentation process. As mentioned before, due the required user input, namely defining the

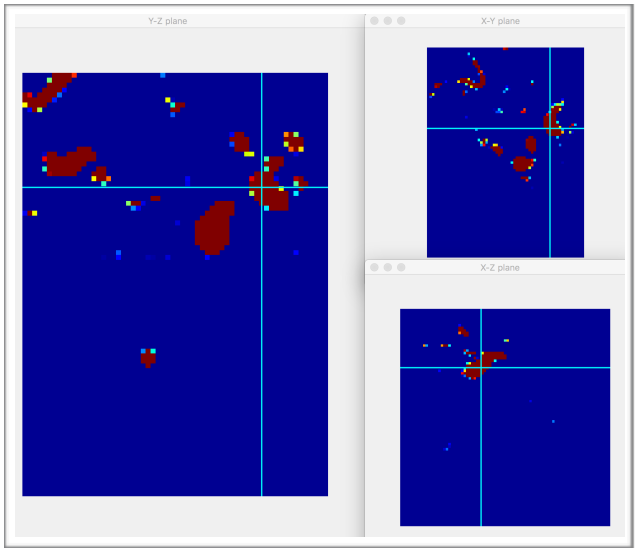


Figure 3.10: Orthogonal slice views generated using script adapted from L. Balkay, 2009.

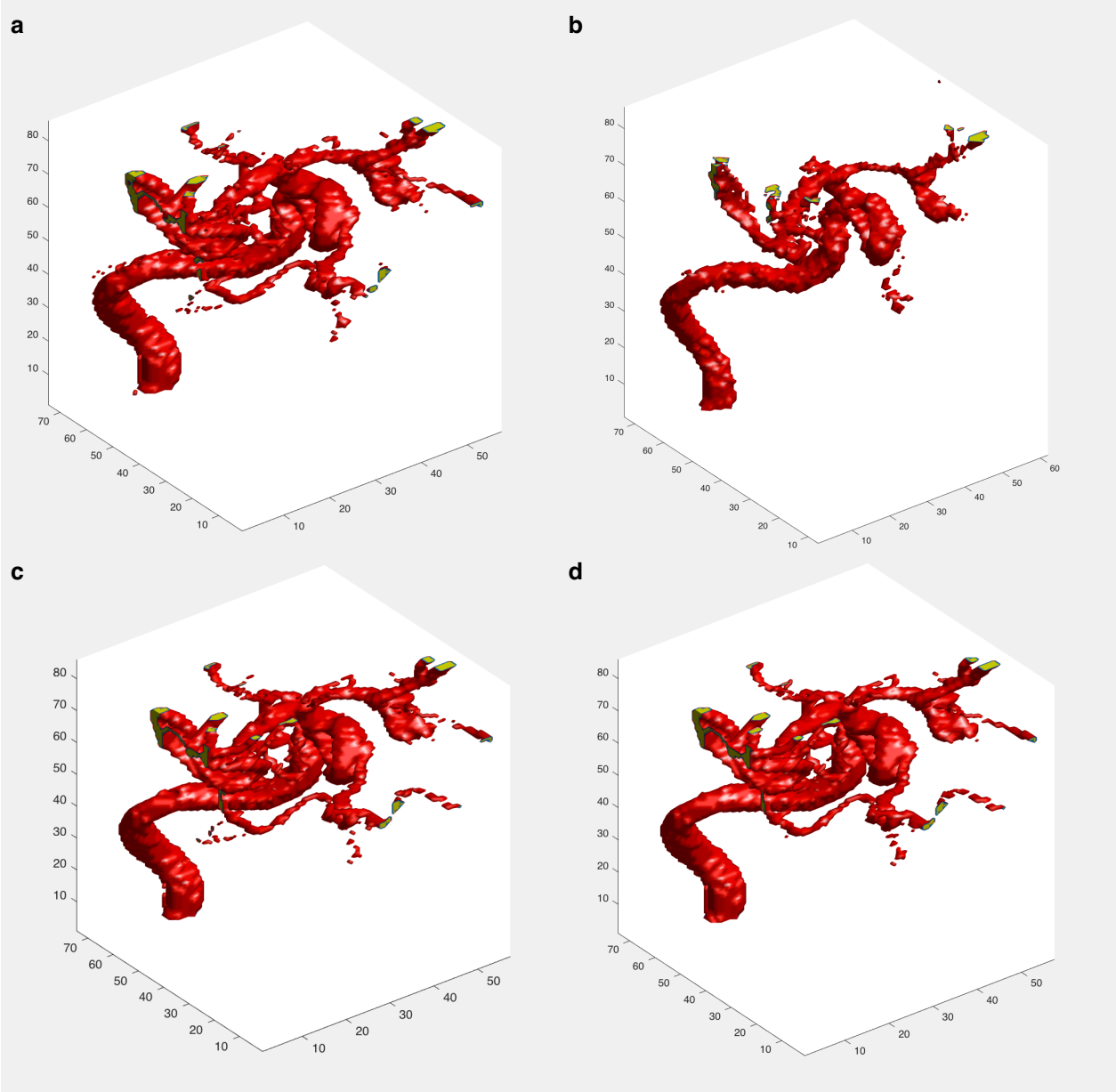


Figure 3.12: the effect on the segmentation results with different modifier values: (a) $m = 1$, (b) $m = 2$, (c) $m = 0.5$, and (d) $m = 0.05$.

seed point or starting voxel, this algorithm is semi-automatic. No additional user input is required and once complete the script outputs a new image stack containing only the segmented features and creates a 3-D surface plot so that the user is able to verify the output. Figure 3.11 shows an example surface rendering of the segmented volume. It is possible to notice some discontinuity and roughness in the image. This is partly due to the rendering and does not reflect the actual data and in part due to errors in the segmentation process.

In an attempt to improve the accuracy of the segmentation algorithm a new parameter was added, called a modifier to the segmentation mask. This modifier m is a scalar value which is multiplied to the mask in order to change the threshold value for all neighbouring pixels in proportion. A value of 1 for the modifier m leaves the mask unmodified and produces the same result as without the modifier. Figure 3.12 shows the effect on the segmentation results with different modifier values: (a) $m = 1$, (b) $m = 2$, (c) $m = 0.5$, and (d) $m = 0.05$. Evidently, values for m greater than 1 produce aberrant results with drastic topography changes characterised particularly by thinning of smaller vessels, disconnection and overall loss of features. Values for m lesser than 1 result in significant improvement in segmentation. At $m = 0.5$ the improvement is modest and can be seen in particular in the ophthalmic artery and smaller branches of the anterior cerebral artery. An even smaller value of $m = 0.05$ provides much better results, however, further reductions do not show any significant difference in segmentation accuracy; a saturation behaviour seems to develop at approximately $m = 0.05$. The m value would likely serve as an adequate variable to adjust depending on the origin modality for the images used in segmentation. That is to say, if a MRA stack is used, the m value could potentially be the only variable that needs changing in order to obtain adequate results. A rapid test of this hypothesis was performed using a MRA stack and the resulting image is shown in Figure 3.13. Notice that the general anatomy is well extracted and

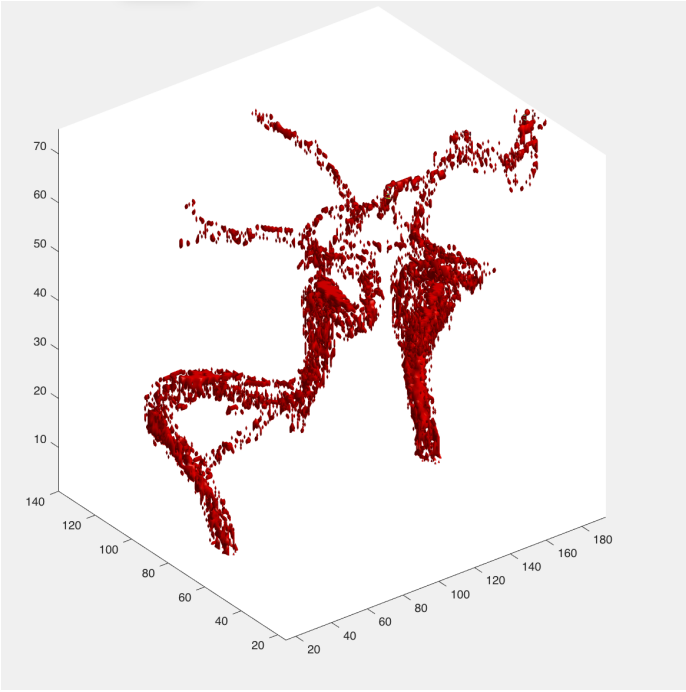


Figure 3.13: Example segmentation of a MRA stack.

preserved despite the overall disconnection of the voxels. Modification of the *m* value was attempted to obtain better results however the general fragmentation of the resultant volume remained and was not significantly reduced. This however can easily be corrected by using a series of morphological operation to close the gaps between voxels. As this work focuses on the extraction of the cerebral angioarchitecture from DSA images, additional work on vessel segmentation from different modalities was not performed.

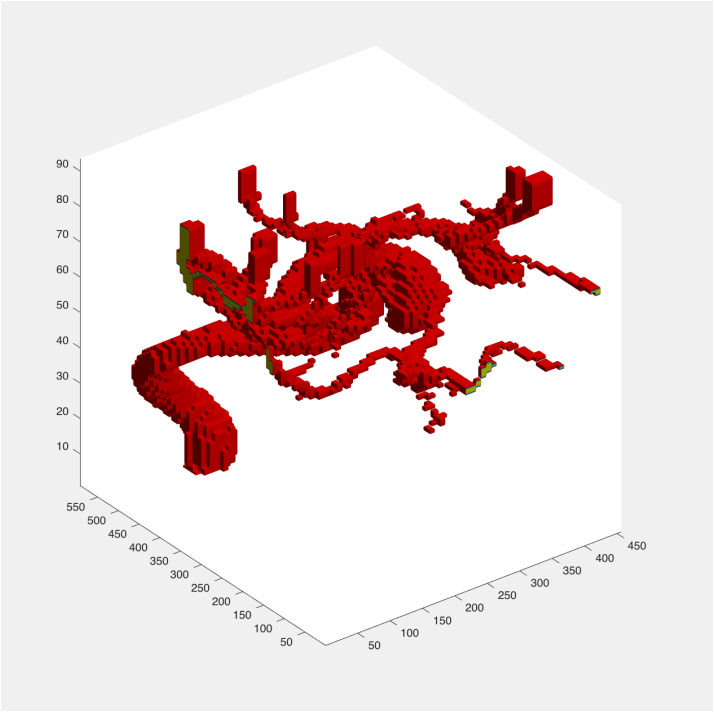


Figure 3.14: Vocalised volume result of segmentation programme.

Meshing of segmented volume

Due to the nature of the original data and the segmentation method used, the resultant segmented volume is voxelised and hence the edges are not smooth. The reconstructions shown in, for example Figure 3.11, is a volume rendering that creates a smoothed image when in reality the data is still made up of discrete voxels and therefore the surface is not regular as can be seen in Figure 3.14. There exist a multitude of methods to smooth the voxelised volume, nevertheless, as it is necessary to export the segmented volume as a mesh, the best alternative is to, in one process, convert the volume into a mesh [90]. A mesh is a representation of the surface of a volume by creating multiple nodes along the surface which when connected from a series of

triangles along the surface. The information is simply encoded as the location of the nodes which permits a variety of programmes to easily reconstruct the surface. There exist multiple methods of meshing both surfaces and volumes and although a simple triangular surface mesh was elected in this particular case it should be noted that other alternatives such as tetrahedral, octree, polyhedral, and others are available and are better suited for volume mesh applications where variation of resolution is required particularly along the boundaries. Tabor et al. [91] classify mesh generation into CAD-type approaches and voxel-based approaches. The former involves generating a surface and then discretising it. As the authors, state this method results in reduced accuracy in determining the bounding surface. Voxel-based methods, on the other hand, uses the pixelised data to generate a mesh of the entire volume. Young, et al., for example compare a novel method called enhanced volumetric marching cubes to conventional and widely available methods [92]. Focus is on processing speed and accuracy to determine the efficiency of these methods in addition to more subjective analysis by means of surface or volume renderings of the resultant mesh.

A simple method of creating a triangular mesh is by exporting the volume as a stereolithography or STL file which requires a meshing step [93]. Generating STL files for segmented volumes is of particular use for both 3D printing or rapid prototyping as well as computer fluid dynamics simulations and other modelling techniques [68]. In order to mesh the volume, code from A.H. Aitkenhead was used and modified to receive the voxelised geometry and output a STL file containing the geometry. To ensure that the resulting volume is produced with adequate preservation of measurements and more importantly the proportions, the meshing programme's code was altered to uses input from the DICOM metadata. Moreover, the code was modified to permit smoothing along the surface of the volume and hence prevent the mesh from

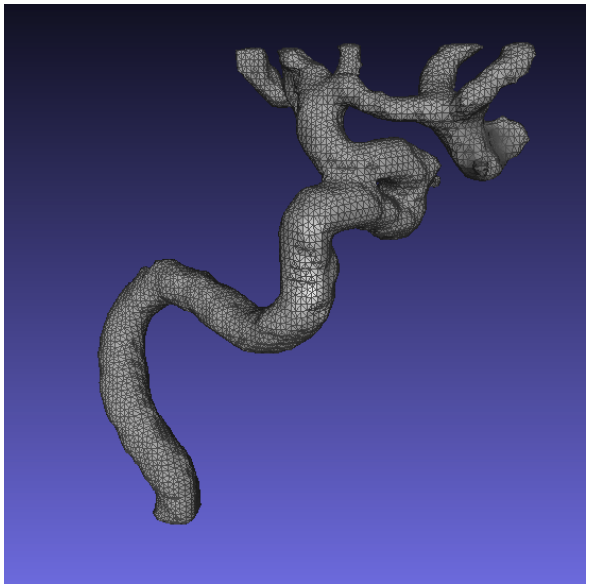


Figure 3.15: Meshed volume using code based on A.H. Aitkenhead [96].

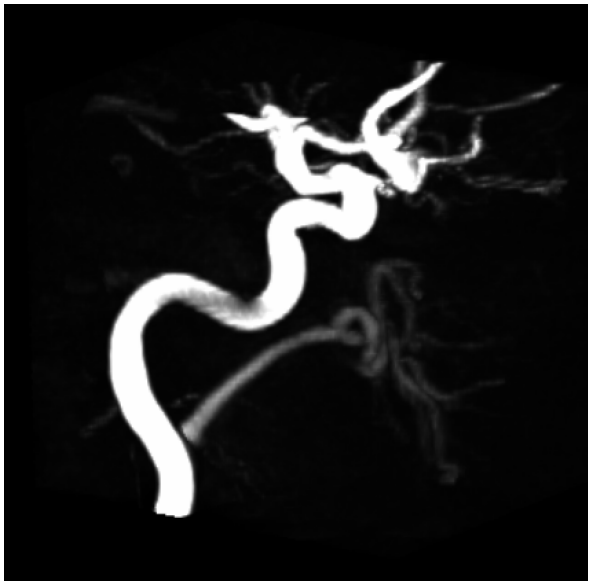


Figure 3.16: Maximum intensity projection of DSA image stack.

conforming perfectly to the right angles on the surface made by individual vowels. The result of such meshing can be seen in Figure 3.15 as viewed in the freeware CAD software MeshLab.

Accuracy test for segmentation algorithm

In order to determine the efficacy of the segmentation algorithm, measurements were performed on both the resulting volume as well as on a maximum intensity projection of the original stack and then compared as was done for the example two-dimensional image segmentation test. The pairs of measurements were again analysed using a non-parametric Wilcoxon matched-pairs signed rank test for continuous variables. A *P*-value of 0.0932 was obtained and it can therefore be assumed that the measurements are not significantly different. The linear regression of the data shown in Figure 3.17 results in a slope of 0.9223 ± 0.008764 with an R^2 value of 0.9102. Again, the sum of the ratio of the differences between the measurements in the original image and the segmented image was 0.0063 or 0.63% which indicates a significantly high correlation between the paired measurements. It should be

mentioned that this test is susceptible to variation as measurements in the MIP image (Figure 3.16) require an approximate determination of the vessel boundary in order to determine the diameter. Once again, the results above show that the segmentation causes negligible decimation or dilation of the segmented area. Nevertheless, reviewing the resultant volume globally, there is evidence of kissing vessels. This is particularly evident in the merger of the cavernous and paraopthalmic segments of the internal carotid artery. Currently, this is a common problem with this segmentation technique and is also commonly seen in other segmentation algorithms as the separation between these two segments before and after the clinoid loop is narrow and the space is only taken by the cavernous sinus, a venous network in the base of the skull that is bound to contain a certain amount of contrast after a bolus injection [16].

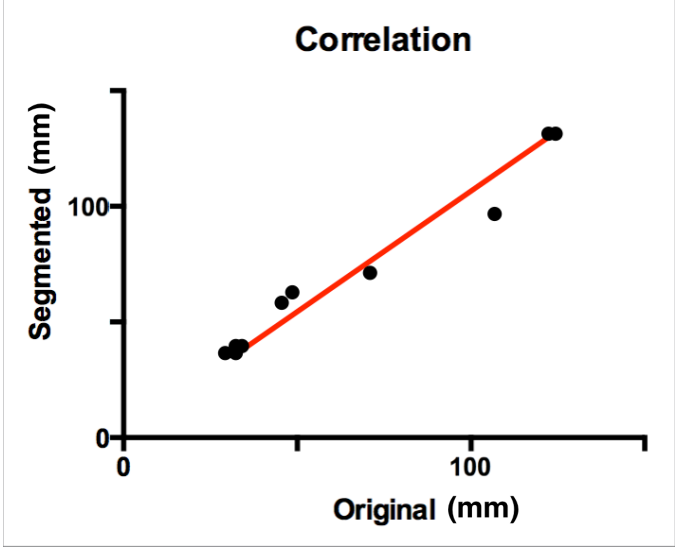


Figure 3.17: Linear regression of paired measurements in millimetres taken from the original image and the corresponding measurement in the segmented image.

Although the current segmentation technique described has yet to be improved it shows promising results that with refinement will lead to an efficient and accurate method for isolating the cerebral angioarchitecture from DSA images as well as other modalities with further alterations.

Chapter 4: Discussion & Conclusion

As has been described in this work, image segmentation is a useful technique in image processing in various fields. In medicine it permits the visualisation of isolated parts of the anatomy in isolation as well as extracting these as volumes for applications such as rapid prototyping, finite element methods and computer fluid dynamics. Although numerous methods for vessel segmentation from medical images exist, no single method is able to accurately and efficiently produce results from any input modality and for any particular anatomy. This is due to the fact that these algorithms all exploit assumptions on the image properties of the specific feature of choice including image intensity values or geometric properties. These criteria are then compounded into a model that is used to drive the algorithms decision making process to determine whether or not a certain region of the image contains the feature of interest [50].

The extraction method described in this work assumes that the contrast contained inside the vessels is of higher intensity than the surrounding background and in consequence uses an initial thresholding procedure to intensify the difference between the vessel features and non-vessel background. A series of image crops in two orthogonal planes across the entire stack reduce the file size and further eliminate vessels that are not of interest. This step helps reduce the processing time required for the actual segmentation step. Subsequently, the segmentation algorithm requires user input in the form of a seed point within the vessel of interest. Automatically, the programme begins to compare neighbouring voxels with the seed voxel in order to determine the probability that they are in fact part of the same feature based on the ratio difference of intensity values and using a lookup mask that defines the values for each of the 26 neighbouring voxels based on the geometric interaction between a sphere and a cubic grid. Once voxels have been included in the feature, the algorithm iteratively compares these newly included

voxels with its neighbours. The programme continues throughout the image until it has analysed all voxels or is no longer able to add voxels to the extracted feature of interest with additional iterations. As the data is voxelised before processing and the output remains in grid format after segmentation it is necessary to mesh the data. This was done by adapting code from A.H. Aitkenhead for MatLab to mesh the surface of the voxelised volume and create a STL file containing this surface.

The overall results of the segmentation technique described are suitable, nevertheless, kissing vessels are still present and reflects the most important inaccuracy of this method of segmentation and should be addressed with the upmost priority. It must also be noted that at least in part, this error is due to the boundary inaccuracies inherent of CAD-based meshing [91]. This can be done by either combining centreline extraction with ray casting or by changing the moving mask in order to detect edges better even when vessel edges are in apposition as may be the case along the clinoid loop. An adaptation might involve changing the values in the mask, which currently represent difference ratios in voxel intensity values to gradients, or rather using a gradient plot of the image and using an adapted moving mask to determine voxels to be included in the segmented volume according to gradient differences in the image which should permit a better determination of vessel edges whilst still using the novel three-dimensional moving mask method presented in this work [57]. Using the gradient plot it may be possible to determine edges better. In addition, there are no restrictions on how many methods for the moving mask are used or what modifiers are implemented with this algorithm. Hence, it is feasible that a number of masks are used in either multiple passes or simultaneously to determine the probability that a neighbouring voxels contains the feature found in the seed voxel. Nevertheless, additional segmentation techniques should probably be incorporated, such as centreline detection and ray

casting as was mentioned previously, in order to increase the accuracy of the technique. Determining the centreline spline could also be useful for later applications of the segmented volume, for example in the virtual deployment of stents [68] [94].

The work presented shows that the moving mask method is a promising new technique for medical image segmentation. The preliminary results are adequate but do exhibit typical errors found in other segmentation methods used for vessels. Further work should focus on refining the moving mask method to include a gradient intensity comparison mask rather than a simple intensity mask as well as optimising the algorithm to be faster. Speed is essential in this application as the intended purpose of segmenting vessels in DSA images is to allow the interventionist to easily plan and possibly simulate treatment inside the angiography room and during the procedure.

Chapter 5: Bibliography

[1] R. Porter, *The Greatest Benefit to Mankind: A Medical History of Humanity (The Norton History of Science)*. 1999.

[2] F. A. Pattie, *Mesmer and animal magnetism: A chapter in the history of medicine.* Edmonston Publishing, 1994.

[3] M. Irfan, R. Waldron, J. Bolger, and K. Barry, "Transillumination: shining a light from within.," *BMJ Case Rep*, vol. 2014, 2014.

[4] O. Glasser, *Wilhelm Conrad Röntgen and the Early History of the Roentgen Rays - Otto Glasser - Google Books*. 1993.

[5] F. KNUTSSON, "Rontgen and Nobel-Prize - Discussion at Royal-Swedish-Academy-of-Sciences in Stockholm in 1901," *Acta Radiol Diagn (Stockh)*, vol. 15, no. 5, pp. 465–473, 1974.

[6] V. Halbach, R. Higashida, and G. Hieshima, "Interventional Neuroradiology," *American Journal of Roentgenology*, vol. 153, no. 3, pp. 467–476, Sep. 1989.

[7] S. Lakhan, A. Kaplan, C. Laird, and Y. Leiter, "The interventionalism of medicine: interventional radiology, cardiology, and neuroradiology," *Int Arch Med*, vol. 2, no. 1, p. 27, 2009.

[8] E. Moniz, "L'encéphalographie artérielle, son importance dans la localisation des tumeurs cérébrales.," *Rev Neurol*, vol. 2, pp. 72–89, 1927.

[9] A. Engeset, "Cerebral angiography with perabrodil (carotis angiography).," *Acta radiol*, vol. Suppl, p. 61, 1944.

[10] S. Seldinger, "Catheter replacement of the needle in percutaneous arteriography; a new technique," *Acta radiol*, vol. 39, no. 5, pp. 368–376, 1953.

[11] S. Wolpert, "On the radiologic-diagnosis of cerebral aneurysms with plain films and cerebral-angiography - A historical survey," *AMERICAN JOURNAL OF NEURORADIOLOGY*, vol. 16, no. 1, pp. 181–184, 1995.

[12] J. Bull, "Contribution of radiology to the study of intracranial aneurysms," *Br Med J*, vol. 2, no. 5321, pp. 1701–1708, 1962.

[13] L. Goertz, "Monte Carlo simulation of a prototypical patient dosimetry system for fluoroscopic procedures."

[14] G. M. Teasdale, D. M. Hadley, A. Lawrence, I. Bone, H. Burton, R. Grant, B. Condon, P. Macpherson, and J. Rowan, "Comparison of magnetic resonance imaging and computed tomography in suspected lesions in the posterior cranial fossa.," *BMJ*, vol. 299, no. 6695, pp. 349–355, Aug. 1989.

[15] A. Setton, A. Davis, A. Bose, P. Nelson, and A. Berenstein, "Angiography of cerebral aneurysms," *Neuroimaging Clinics of North America*, vol. 6, no. 3, pp. 705–&, 1996.

[16] I. Wächter, "3D reconstruction of cerebral blood flow and vessel morphology from X-ray rotational angiography," 2009.

[17] A. Filler, "The history, development, and impact of computed imaging in neurological diagnosis and neurosurgery:CT, MRI, and DTI," *Nature Precedings*, 2009.

[18] R. Hashemi, W. Bradley, and C. Lisanti, *MRI: The Basics*. 2004.

[19] M. Bettmann, "Angiographic Contrast Agents - Conventional and New Media Compared," *American Journal of Roentgenology*, pp. 787–794, 1982.

[20] R. Hurst and R. Rosenwasser, *Interventional neuroradiology*. 2008, pp. xi, 420 p.–420 p.

[21] V. Janardhan and A. Qureshi, “Advances in interventional neuroimaging,” *Neurotherapeutics*, vol. 4, pp. 414–419, 2007.

[22] T. Sugahara, Y. Korogi, K. Nakashima, S. Hamatake, S. Honda, and M. Takahashi, “Comparison of 2D and 3D digital subtraction angiography in evaluation of intracranial aneurysms.,” *AMERICAN JOURNAL OF NEURORADIOLOGY*, vol. 23, no. 9, pp. 1545–1552, Oct. 2002.

[23] P. Turski, M. Steighorst, C. Strother, A. Crummy, J. Sackett, and R. Lieberman, “Digital subtraction arteriography (DSA) mapping - An angiographic tool,” *American Journal of Roentgenology*, pp. 430–430, 1982.

[24] P. Turski, M. Stieghorst, C. Strother, A. Crummy, R. Lieberman, and C. Mistretta, “Digital subtraction arteriography road map,” *American Journal of Roentgenology*, pp. 1233–1234, 1982.

[25] R. Anxionnat, S. Bracard, X. Ducrocq, Y. Trousset, L. Launay, E. Kerrien, M. Braun, R. Vaillant, F. Scomazzoni, A. Lebedinsky, and L. Picard, “Intracranial Aneurysms: Clinical Value of 3D Digital Subtraction Angiography in the Therapeutic Decision and Endovascular Treatment1,” *RADIOLOGY*, vol. 218, no. 3, pp. 799–808, Mar. 2001.

[26] S. Tateshima, Y. Murayama, J. Villablanca, T. Morino, H. Takahashi, T. Yamauchi, K. Tanishita, and F. Vinuela, “Intraaneurysmal flow dynamics study featuring an acrylic aneurysm model manufactured using a computerized tomography angiogram as a mold,” *JOURNAL OF NEUROSURGERY*, pp. 1020–1027, Oct. 2001.

[27] F. Runck, R. Steiner, W. Bautz, and M. Lell, “MR Imaging: Influence of Imaging Technique and Postprocessing on Measurement of Internal Carotid Artery Stenosis,” *AMERICAN JOURNAL OF NEURORADIOLOGY*, pp. 1736–1742, Aug. 2008.

[28] S. Maderwald, S. Ladd, E. Gizewski, O. Kraff, J. Theysohn, K. Wicklow, C. Moenninghoff, I. Wanke, M. Ladd, and H. Quick, “To TOF or not to TOF: strategies for non-contrast-enhanced intracranial MRA at 7 T,” *MAGNETIC RESONANCE MATERIALS IN PHYSICS BIOLOGY AND MEDICINE*, pp. 159–167, Jan. 2008.

[29] M. Zhao, F. Charbel, N. Alperin, F. Loth, and M. Clark, “Improved phase-contrast flow quantification by three-dimensional vessel localization,” *MAGNETIC RESONANCE IMAGING*, pp. 697–706, May 2000.

[30] M. Vermandel, N. Betrouni, C. Taschner, C. Vasseur, and J. Rousseau, “From MIP image to MRA segmentation using fuzzy set theory,” *COMPUTERIZED MEDICAL IMAGING AND GRAPHICS*, pp. 128–140, Feb. 2007.

[31] J. Brisman, Y. Niimi, J. Song, and A. Berenstein, “Aneurysmal rupture during coiling: Low incidence and good outcomes at a single large volume center,” *Neurosurgery*, vol. 57, no. 6, pp. 1103–1108, Dec. 2005.

[32] J. L. Brisman, Y. Niimi, J. K. Song, and A. Berenstein, “Aneurysmal Rupture During Coiling: Low Incidence and Good Outcomes at a Single Large Volume Center,” *Neurosurgery*, vol. 62, no. 6, pp. 1103–1109, Dec. 2005.

[33] N. Heran, J. Song, K. Mamba, W. Smith, Y. Niimi, and A. Berenstein, “The utility of DynaCT in neuroendovascular procedures,” *AMERICAN JOURNAL OF NEURORADIOLOGY*, pp. 330–332, 2006.

[34] A. Pedicelli, M. Rollo, G. Di Lella, T. Tartaglione, C. Colosimo, and L. Bonomo, "3D rotational anglography for the diagnosis and preoperative assessment of intracranial aneurysms: preliminary experience," *Radiologia Medica*, vol. 112, no. 6, pp. 895–905, Sep. 2007.

[35] Y. Kyriakou, T. Struffert, A. Dorfler, and W. Kalender, "Basics priciples of flat detector computed tomography (FD-CT)," *Radiologe*, vol. 49, no. 9, pp. 811–819, Sep. 2009.

[36] W. J. van Rooij, M. E. Sprengers, A. N. de Gast, J. P. P. Peluso, and M. Sluzewski, "3D Rotational Angiography: The New Gold Standard in the Detection of Additional Intracranial Aneurysms," *AJNR Am J Neuroradiol*, vol. 29, no. 5, pp. 976–979, Feb. 2008.

[37] S. Tanoue, H. Kiyosue, H. Kenai, T. Nakamura, M. Yamashita, and H. Mori, "Three-dimensional reconstructed images after rotational angiography in the evaluation of intracranial aneurysms: Surgical correlation," *Neurosurgery*, pp. 866–871, Aug. 2000.

[38] M. Castro, C. Putman, and J. Cebral, "Computational modeling of cerebral aneurysms in arterial networks reconstructed from multiple 3D rotational angiography images," *Medical Imaging 2005: Physiology, Function, and Structure From Medical Images, Pts 1 and 2*, pp. 233–244, 2005.

[39] M. Castro, C. Putman, and J. Cebral, "Patient-specific computational modeling of cerebral aneurysms with multiple avenues of flow from 3D rotational angiography images," *ACADEMIC RADIOLOGY*, pp. 811–821, May 2006.

[40] T. Hassan, E. Timofeev, T. Saito, H. Shimizu, M. Ezura, T. Tominaga, A. Takahashi, and K. Takayama, "Computational replicas: Anatomic reconstructions of cerebral vessels as volume numerical grids at three-dimensional angiography," *AMERICAN JOURNAL OF NEURORADIOLOGY*, pp. 1356–1365, Jul. 2004.

[41] F. Duck, A. Baker, and H. Starritt, *Ultrasound in medicine*. 1998, pp. xxxi, 314 p.–314 p.

[42] D. Steinman, "Image-based computational fluid dynamics modeling in realistic arterial geometries," *Ann Biomed Eng*, pp. 483–497, Feb. 2002.

[43] L. Tartaglino and R. Gorniak, "Advanced Imaging Applications for Endovascular Procedures," *Neurosurgery Clinics of North America*, vol. 20, no. 3, pp. 297–+, Jul. 2009.

[44] Z. Arthurs, B. Starnes, V. Sohn, N. Singh, and C. Andersen, "Ultrasound-Guided Access Improves Rate of Access-Related Complications for Totally Percutaneous Aortic Aneurysm Repair," *ANNALS OF VASCULAR SURGERY*, vol. 22, no. 6, pp. 736–741, 2008.

[45] A. Samal and C. White, "Percutaneous management of access site complications," *Catheterization and Cardiovascular Interventions*, vol. 57, no. 1, pp. 12–23, 2002.

[46] D. Dausch, J. Castellucci, D. Chou, and O. von Ramm, " Piezoelectric Micromachined Ultrasound Transducer (pMUT) Arrays for 3D Imaging Probes.," *2006 IEEE Ultrasonics Symposium Proceedings*, vol. 1, pp. 934–937, 2006.

[47] O. Demirkaya, M. Asyali, and P. Sahoo, *Image processing with MATLAB : applications in medicine and biology*. 2009, pp. xv, 441 p.–441 p.

[48] V. L. Roger, A. S. Go, D. M. Lloyd-Jones, E. J. Benjamin, J. D. Berry, W. B. Borden,

D. M. Bravata, S. Dai, E. S. Ford, and C. S. Fox, “Heart Disease and Stroke Statistics--2012 Update: A Report From the American Heart Association.,” *Circulation*, 2011.

[49] C. Kirbas and F. Quek, “A review of vessel extraction techniques and algorithms,” *ACM Comput. Surv.*, vol. 36, no. 2, pp. 81–121, Jun. 2004.

[50] D. Lesage, E. D. Angelini, I. Bloch, and G. Funka-Lea, “A review of 3D vessel lumen segmentation techniques: models, features and extraction schemes.,” *Med Image Anal*, vol. 13, no. 6, pp. 819–845, Dec. 2009.

[51] D. L. Wilson and J. A. Noble, “An adaptive segmentation algorithm for time-of-flight MRA data.,” *IEEE Trans. Med. Imaging*, vol. 18, no. 10, pp. 938–945, Sep. 1999.

[52] A. F. Frangi, W. J. Niessen, R. M. Hoogeveen, T. van Walsum, and M. A. Viergever, “Model-based quantitation of 3-D magnetic resonance angiographic images.,” *IEEE Trans. Med. Imaging*, vol. 18, no. 10, pp. 946–956, Oct. 1999.

[53] Y. Cheng, X. Hu, J. Wang, Y. Wang, and S. Tamura, “Accurate Vessel Segmentation With Constrained B-Snake,” *IEEE Transactions on Image Processing*, vol. 24, no. 8, pp. 2440–2455, 2015.

[54] M. Rochery, “Contours actifs d´ ordre supérieur et leur application à la détection de linéiques dans des images de télédétection,” 2005.

[55] Y. Fridman, S. M. Pizer, S. Aylward, and E. Bullitt, “Segmenting 3D Branching Tubular Structures Using Cores,” in *Medical Image Computing and ...*, vol. 2879, no. 70, Berlin, Heidelberg: Springer Berlin Heidelberg, 2003, pp. 570–577.

[56] J. Lee, P. Beighley, E. Ritman, and N. Smith, “Automatic segmentation of 3D micro-CT coronary vascular images.,” *Med Image Anal*, vol. 11, no. 6, pp. 630–647, Dec. 2007.

[57] J. Canny, “A computational approach to edge detection.,” *IEEE Trans Pattern Anal Mach Intell*, vol. 8, no. 6, pp. 679–698, Jun. 1986.

[58] M. Akif Gulsun and H. Tek, “Geometric modeling of tubular structures,” presented at the Computer Vision and Pattern Recognition Workshops, 2008. CVPRW '08. IEEE Computer Society Conference on, 2008, pp. 1–8.

[59] N. Armande, P. Montesinos, and O. Monga, “Thin nets extraction using a multi-scale approach,” *Computer Vision and ...*, 1999.

[60] M. P. Chwialkowski, Y. M. Ibrahim, H. F. Li, and R. M. Peshock, “A method for fully automated quantitative analysis of arterial flow using flow-sensitized MR images.,” *Comput Med Imaging Graph*, vol. 20, no. 5, pp. 365–378, Sep. 1996.

[61] T. Boskamp, D. Rinck, F. Link, B. Kümmerlen, G. Stamm, and P. Mildenberger, “New vessel analysis tool for morphometric quantification and visualization of vessels in CT and MR imaging data sets.,” *Radiographics*, vol. 24, no. 1, pp. 287–297, Jan. 2004.

[62] J. Yi and J. B. Ra, “A locally adaptive region growing algorithm for vascular segmentation,” *Int. J. Imaging Syst. Technol.*, vol. 13, no. 4, pp. 208–214, Dec. 2003.

[63] Y. Masutani, T. Schiemann, and K.-H. Höhne, “Vascular shape segmentation and structure extraction using a shape-based region-growing model,” in *Lecture Notes in Computer Science*, vol. 1496, no. 133, Berlin, Heidelberg: Springer Berlin Heidelberg, 2006, pp. 1242–1249.

[64] C. Zahlten, H. Jürgens, C. Evertsz, and R. Leppek, “Portal vein reconstruction based on topology,” *European journal of …*, 1995.

[65] T. McInerney and D. Terzopoulos, “T-snakes: topology adaptive snakes.,” *Med Image Anal*, vol. 4, no. 2, pp. 73–91, Jun. 2000.

[66] O. Wink, W. J. Niessen, and M. A. Viergever, “Fast delineation and visualization of vessels in 3-D angiographic images.,” *IEEE Trans. Med. Imaging*, vol. 19, no. 4, pp. 337–346, Apr. 2000.

[67] G. T. Gullberg and G. L. Zeng, “A cone-beam filtered backprojection reconstruction algorithm for cardiac single photon emission computed tomography.,” *IEEE Trans. Med. Imaging*, vol. 11, no. 1, pp. 91–101, 1992.

[68] T. W. Peach, M. Ngoepe, K. Spranger, D. Zajarias-Fainsod, and Y. Ventikos, “Personalizing flow-diverter intervention for cerebral aneurysms: from computational hemodynamics to biochemical modeling,” *Int. J. Numer. Meth. Biomed. Engng.*, vol. 30, no. 11, pp. 1387–1407, Aug. 2014.

[69] S. Aylward, E. Bullitt, S. Pizer, and D. Eberly, “Intensity ridge and widths for tubular object segmentation and description,” presented at the Mathematical Methods in Biomedical Image Analysis, 1996., Proceedings of the Workshop on, 1996, pp. 131–138.

[70] E. Bullitt and S. Aylward, “Volume Rendering of Segmented Tubular Objects,” in *Medical Image Computing and Computer-Assisted …*, vol. 2208, no. 20, Berlin, Heidelberg: Springer Berlin Heidelberg, 2001, pp. 161–168.

[71] Y. Wang and P. Liatsis, “IEEE Xplore Abstract - Automatic Segmentation of Coronary Arteries in CT Imaging in the Presence of Kissing Vessel Artifact...,” *Information Technology in Biomedicine*, 2012.

[72] H. Ujiie, H. Tachibana, O. Hiramatsu, A. Hazel, T. Matsumoto, Y. Ogasawara, H. Nakajima, T. Hori, K. Takakura, and F. Kajiya, “Effects of size and shape (aspect ratio) on the hemodynamics of saccular aneurysms: A possible index for surgical treatment of intracranial aneurysms,” *Neurosurgery*, vol. 45, no. 1, pp. 119–129, 1999.

[73] G. Espinosa, L. Dzieciuchowicz, and L. Grochowicz, “Endovascular Treatment of Carotid Stenosis Associated with Incidental Intracranial Aneurysm,” *ANNALS OF VASCULAR SURGERY*, pp. –, Sep. 2009.

[74] M. Nair, J. Pettigrew, and A. Mancuso, “Intracranial aneurysm as an incidental finding,” *DENTOMAXILLOFACIAL RADIOLOGY*, pp. 107–112, 2007.

[75] B. Weir, L. Disney, and T. Karrison, “Sizes of ruptured and unruptured aneurysms in relation to their sites and the ages of patients,” *JOURNAL OF NEUROSURGERY*, pp. 64–70, 2002.

[76] D. Wiebers, J. Whisnant, J. Huston, I. Meissner, R. Brown, D. Piepgras, G. Forbes, K. Thielen, D. Nichols, W. O'Fallon, J. Peacock, L. Jaeger, N. Kassell, G. Kongable-Beckman, J. Torner, A. Naleway, B. Yoo, B. Sorensen, D. Wiebers, C. Drake, G. Ferguson, J. Kurtzke, A. Andreoli, G. Edner, R. Sengupta, J. Castel, A. Molyneux, J. Marler, and I. Intracranial, “Unruptured intracranial aneurysms: natural history, clinical outcome, and risks of surgical and endovascular treatment,” *LANCET*, pp. 103–110, Jul. 2003.

[77] T.-M. Liou and S.-N. Liou, “A review on in vitro studies of hemodynamic

characteristics in terminal and lateral aneurysm models," *Proceedings of the National Science Council Republic of China Part B Life Sciences*, vol. 23, no. 4, pp. 133–148, 1999.

[78] D. Steinman, J. Milner, C. Norley, S. Lownie, and D. Holdsworth, "Image-based computational simulation of flow dynamics in a giant intracranial aneurysm," *AMERICAN JOURNAL OF NEURORADIOLOGY*, pp. 559–566, Feb. 2003.

[79] D. Zajarias-Fainsod, A. Wilson, and J. Collingwood, "Viability of a patient-specific fluid-dynamics modelling approach in the treatment of intracranial aneurysms.," 2010.

[80] J. Jiang, K. Johnson, K. Valen-Sendstad, K.-A. Mardal, D. Consigny, O. Wieben, and C. Strother, "Comparison of Aneurismal Hemodynamics Between 4-D Accelerated Phase-Contrast MR Angiography and Computational Fluid Dynamics Simulations: Initial Experience in a Canine Aneurysm Model," presented at the ASME 2010 Summer Bioengineering Conference, 2010, p. 223.

[81] S. Rhode, M. Paul, E. Martens, and D. F. Campbell, "Blood flow dynamics in patient specific arterial network
in head and neck," Mar. 2011.

[82] J. A. Moore, D. A. Steinman, and C. Ross Ethier, "Computational blood flow modelling," *J Biomech*, vol. 31, no. 2, pp. 179–184, May 1997.

[83] M. Piotin, P. Gailloud, L. Bidaut, S. Mandai, M. Muster, J. Moret, and D. A. Rüfenacht, "CT angiography, MR angiography and rotational digital subtraction angiography for volumetric assessment of intracranial aneurysms. An experimental study.," *Neuroradiology*, vol. 45, no. 6, pp. 404–409, Jun. 2003.

[84] K. Namba, Y. Niimi, J. K. Song, and A. Berenstein, "Use of Dyna-CT Angiography in Neuroendovascular Decision-Making. A Case Report.," *Interv Neuroradiol*, vol. 15, no. 1, pp. 67–72, Mar. 2009.

[85] I. K. Indrajit and B. S. Verma, "Monitor displays in radiology: Part 2.," *Indian J Radiol Imaging*, vol. 19, no. 2, pp. 94–98, Apr. 2009.

[86] P. Mildenberger, M. Eichelberg, and E. Martin, "Introduction to the DICOM standard.," *Eur Radiol*, vol. 12, no. 4, pp. 920–927, Apr. 2002.

[87] F. Gijsen, E. Allanic, and F. N. Van de Vosse, "The influence of the non-Newtonian properties of blood on the flow in large arteries: unsteady flow in a 90 curved tube," *Journal of ...*, 1999.

[88] N. Sang, H. Li, W. Peng, and T. Zhang, "Knowledge-based adaptive thresholding segmentation of digital subtraction angiography images," *Image and Vision Computing*, 2007.

[89] T. Hirai, Y. Korogi, H. Arimura, S. Katsuragawa, M. Kitajima, M. Yamura, Y. Yamashita, and K. Doi, "Intracranial Aneurysms at MR Angiography: Effect of Computer-aided Diagnosis on Radiologists' Detection Performance 1," *RADIOLOGY*, vol. 237, no. 2, pp. 605–610, Nov. 2005.

[90] J. R. Cebral and R. Löhner, "From medical images to anatomically accurate finite element grids," *Int. J. Numer. Meth. Engng.*, vol. 51, no. 8, pp. 985–1008, Jul. 2001.

[91] G. Tabor, D. Tame, F. Pierron, P. G. Young, A. Watkinson, and J. Thompson, *Patient-Specific Arterial Flow Simulation with Additional Geometric Elements*. Delft University of Technology; European Community on Computational Methods in

Applied Sciences (ECCOMAS), 2006.

[92] P. G. Young, T. B. H. Beresford-West, S. R. L. Coward, B. Notarberardino, B. Walker, and A. Abdul-Aziz, “An efficient approach to converting three-dimensional image data into highly accurate computational models,” *Philosophical Transactions of the Royal Society of London A: Mathematical, Physical and Engineering Sciences*, vol. 366, no. 1878, pp. 3155–3173, Sep. 2008.

[93] A. Marro, T. Bandukwala, and W. Mak, “Three-Dimensional Printing and Medical Imaging: A Review of the Methods and Applications.,” *Curr Probl Diagn Radiol*, vol. 45, no. 1, pp. 2–9, Jan. 2016.

[94] R. P. Kumar, F. Albregtsen, M. Reimers, B. Edwin, T. Langø, and O. J. Elle, “Three-Dimensional Blood Vessel Segmentation and Centerline Extraction based on Two-Dimensional Cross-Section Analysis.,” *Ann Biomed Eng*, vol. 43, no. 5, pp. 1223–1234, Apr. 2015.

[95] Pham, Dzung L.; Xu, Chenyang; Prince, Jerry L. (2000). "Current Methods in Medical Image Segmentation". Annual Review of Biomedical Engineering 2: 315–337.

[96] A. Aitkenhead, “Mesh voxelisation - File Exchange - MATLAB Central,” mathworks.com. [Online]. Available: https://www.mathworks.com/matlabcentral/fileexchange/27390-mesh-voxelisation. [Accessed: 25-Jul-2015].

Appendix A: MatLab Code

DICOM Load

```
function [I, width, height, depth, voxelsize] = dicomload()
% make sure that voxelsize and/or the metadata is kept for use later

%% Locates DICOM Files using basic GUI
folder = uigetdir;
directory = dir(fullfile(folder, '*.dcm'));
cd(folder);

%% Reads first DICOM file metadata and determines image and stack size

depth = length(directory); % stack size
dcm1 = directory(1).name; % first file in the stack
info = dicominfo(dcm1);  % loads the metadata for the first file
width = info.Width;    % width dimension
height = info.Height;   % lenght dimension
voxelsize = [info.PixelSpacing; info.SliceThickness]; % gets voxel size values form
stack (1x3 matrix)

%%

gridX = zeros([1 width]); % prealocates the values for the grid in the x axis
gridY = zeros([1 height]); % prealocates the values for the grid in the y axis
gridZ = zeros([1 depth]); % prealocates the values for the grid in the z axis

% fills in the values for the grid in the x axis
for dx = 1 : width
  gridX(dx) = (single(dx)-1)*voxelsize(1);
end
% fills in the values for the grid in the y axis
for dy = 1 : height
  gridY(dy) = (single(dy)-1)*voxelsize(2);
end
% fills in the values for the grid in the z axis
for dz = 1 : depth
  gridZ(dz) = (single(dz)-1)*voxelsize(3);
end

%% Builds a prealocated 3D matrix with zeros and fills it with patient data.

I = zeros([width height depth]);
bar = waitbar(0,'Loading data. Please wait...');
% writes data into I slice by slice
for dz = 1:depth
  slice = dicominfo(directory(dz).name);
  I(:,:,dz) = dicomread(slice);
  waitbar(dz / depth);
end
close(bar);

I0=I;
```

Enhance (Thresholding)

```
function Jnorm = enhance(I, width, height, depth, voxelsize)
%% Opens an image viewer for the 10th slice so that the user can select the optimal
contrast levels
```

```
preview = imtool(I(:,:,15));
waitfor(preview); %waits for the user to close the image preview above.

%Windows the image and reapplies normalised contrast settings.

prompt = {'Enter lower window threshold:','Enter upper window threshold:'};
dlg_title = 'Window Selection';
num_lines = 1;
def = {'1400','4000'};
window = inputdlg(prompt,dlg_title,num_lines,def); %user inputs window values.

min=str2double(window{1});  %sets the minimum intensity value for the window
max=str2double(window{2});  %sets the maximum intensity value for the window

%I = uint16(I);

%% For the minimum level

%Work out which ones need replacing
%maskOnI = (I(:,:,:)<min);
maskOnI = (I<min);
%create a matrix with all the values to replace the < min values
%valuesToReplace = (maskOnI.*min);
I(maskOnI)= min;

%inverseMaskMatrix = (~maskOnI);
%Set min values to zero
%I = I.*uint16(inverseMaskMatrix);
%Replace the missing min values with values to replace
%I = I + uint16(valuesToReplace);

%% For the maximum level

%Work out which ones need replacing
maskOnI = (I>max);
%create a matrix with all the values to replace the < min values
%valuesToReplace = (maskOnI.*max);
I(maskOnI)= max;

%inverseMaskMatrix = (~maskOnI);
%Set min values to zero
%I = I.*uint16(inverseMaskMatrix);
%Replace the missing min values with values to replace
%I = I + uint16(valuesToReplace);

%% Normalise data

%I = double(I);  %convert 16bit to integers before normalising.

%% Normalises the pixel values to a scale from 0 to 1.

Jnorm = (I-min)/(max-min);  %Subtracts the minimum value from all pixels and then
divides the value by the window width
             %to normalise the pixel values to 1

I=Jnorm;
%% Plots 3D of volume
figure
patch(isocaps(Jnorm,.5),'FaceColor','interp','EdgeColor','none');
p1 = patch(isosurface(Jnorm,.5),'FaceColor','blue','EdgeColor','none');
isonormals(Jnorm,p1)
view(3);
```

```
axis vis3d tight
camlight right
lighting gouraud
```

Cropping

```
%*****************************************************
%In order to identify and focus on the area of interest, the DICOMs are
%cropped. The advantage of copping is to speed up subsequent algorithms.
%The cropping alogrithm is described as follows:

%First, the function, imcrop, is used to draw the area of interest to be
%cropped. (To work the GUI, draw crop rectangle on the orthogonal view of projection
of Jnorm shown and
%select 'Crop image' from the right click menu or double-click after the rectangle has
been drawn).

%% Cropping in the coronal orthogonal view
h = imagesc(rot90(squeeze(sum(I,1))));
colormap(gray);
[I1,rect1]=imcrop(h);
rect1=round(rect1); %makes rectangle dimension into integers
ymin = rect1(1);
ymax = rect1(1)+rect1(3); %represents initial rectangle y-coordinate plus dimension in
y
zmin = size(I,3)-(rect1(2)+rect1(4))+2; %as image is inverted it is necessary to
subtract from maximum dimension.
zmax = size(I,3)-rect1(2); %as image is inverted it is necessary to subtract from
maximum dimension.
% imtool(rot90(squeeze(sum(I(:,ymin:ymax,zmin:zmax),1)))); %used for
% debugging rectangle
Icrop1 = I(:,ymin:ymax,zmin:zmax);

%% Cropping in the sagital orthogonal view

% imtool(rot90(squeeze(sum(Icrop1,2)))); %used for degguing and testing
% previous section
h = imagesc(rot90(squeeze(sum(Icrop1,2))));
colormap(gray);
[I2,rect2]=imcrop(h);
rect2=round(rect2);
xmin = rect2(1);
xmax = rect2(1)+rect2(3); %represents initial rectangle x-coordinate plus dimension in
x
zmin = size(Icrop1,3)-(rect2(2)+rect2(4))+2; %as image is inverted it is necessary to
subtract from maximum dimension.
zmax = size(Icrop1,3)-rect2(2); %as image is inverted it is necessary to subtract from
maximum dimension.
% imtool(rot90(squeeze(sum(Icrop1(xmin:xmax,:,zmin:zmax),2)))); %used for
% debugging rectangle
Icrop2 = Icrop1(xmin:xmax,:,zmin:zmax);
I = Icrop2;

%% Plots 3D of volume

figure
patch(isocaps(Icrop2,.5),'FaceColor','interp','EdgeColor','none');
p1 = patch(isosurface(Icrop2,.5),'FaceColor','blue','EdgeColor','none');
isonormals(Icrop2,p1)
view(3);
```

```
axis vis3d tight
camlight right
lighting gouraud
```

Segmentation (Moving-Mask Volume Growing)

```
orthogonalslicer(I);
waitfor(gca);

prompt = {'x-coordinate:','y-coordinate:','z-coordinate:'};
dlg_title = 'Enter seed voxel coordinates';
num_lines = 1;
coord = inputdlg(prompt,dlg_title,num_lines); %user inputs slice of interest for
seeding.
x = str2double(cell2mat(coord(1)));
y = str2double(cell2mat(coord(2)));
z = size(I,3) - str2double(cell2mat(coord(3))); %z-axis is inverted
%%
%Test that the seed point is not empty
if I(x,y,z) == 0
  h = errordlg('The seed point is empty.','Error');
  waitfor(h);
end

% error threshold to be used when comparing neighbouring pixels.
error(:,:,1) = [.076, .272, .076; .272, .346, .272,; .076, .272, .076];
error(:,:,3) = error(:,:,1);
error(:,:,2) = [.272, .346, .272; .346, 1, .346,; .272, .346, .272];

modifier = .005;

Jlinear = reshape(I,1,[]);
V = zeros(size(I));

queueMask=false(size(I)); %binary masks of voxels left to process
queueMask(x,y,z)=true; %seed
queuelength=nnz(queueMask);
[i,j,k]=meshgrid(1:3,1:3,1:3);
jumps=sub2ind(size(I),i,j,k)-sub2ind(size(I),2,2,2);
totiter = nnz(I)*8;      %estimates total number of iterations;
voxelqueue = [];

h = waitbar(0,'1','Name','Segmenting image. Please
wait...','CreateCancelBtn','setappdata(gcbf,''canceling'',1)');
setappdata(h,'canceling',0)
iter = 0;

while queuelength>0
  % if getappdata(h,'canceling')
  %   break
  % end
  %Vn = size(find(V),1);
  iter = iter+1;
  voxel = find(queueMask,1);
%   disp(['Iteration  ', num2str(voxel)]);
  neighbours = voxel + jumps;
  if sum(ismember(voxelqueue,voxel)) == 0 && ...
      size(find(neighbours > 0),1) == 27 && ...
      nnz(neighbours < size(Jlinear,2)) == 27; %~ismember(neighbours,voxels)
    T=double(Jlinear(neighbours)); %remember to do this (make sure T is positive).
    %sometimes neighbours might be larger than Jlinear
    S=T(14);
```

```
    V(neighbours) = (abs(T - S)/S < error*modifier);
    queueMask(neighbours) = (abs(T - S)/S < error*modifier);
  % elseif sum(ismember(voxelqueue,voxel)) == 0
    %need solution for when some neighbours are <0 ******
  end
  queueMask(voxel)=false;
  queuelength = nnz(queueMask);
  voxelqueue(end+1,:) = voxel;

  waitbar((iter/totiter),h, sprintf('%12.0f',(iter/totiter*100)));
end

delete(h);
I=V;

%% Plots 3D of volume

figure
patch(isocaps(V,.5),'FaceColor','interp','EdgeColor','none');
p1 = patch(isosurface(V,.5),'FaceColor','red','EdgeColor','none');
isonormals(V,p1)
view(3);
axis vis3d tight
camlight right
lighting gouraud
```

Finer Voxels

```
%%finer_voxels is a script that increases the number of voxels in order to augment the
resolution of V
scalefactor = 8;

V2 = imresize(I, scalefactor, 'nearest');

%new script avoids having to concatenate matricies
V3 = zeros(size(V2,1),size(V2,2),(size(V2,3)*scalefactor));
s=1;
  for n = 1:size(I,3)
    for t = 0:(scalefactor-1);
    V3(:,:,n+t) = V2(:,:,n);
    end
  end
V3=V3(:,:,1:(size(V3,3)-scalefactor));

%% Plots 3D of volume

figure
patch(isocaps(V3,.5),'FaceColor','interp','EdgeColor','none');
p1 = patch(isosurface(V3,.5),'FaceColor','red','EdgeColor','none');
isonormals(V3,p1)
view(3);
axis vis3d tight
camlight right
lighting gouraud
```

Smoothing

```
for s=1:size(V,3);
  Vedge(:,:,s)=edge(V(:,:,s),.2);
end
```

```
%%
se=strel('disk',1);
for s=1:size(V,3);
  Verode(:,:,s)=imerode(V(:,:,s),se);
end

%%
se=strel('disk',1);
for s=1:size(V,3);
  Vclose(:,:,s)=imclose(Vclose(:,:,s),se);
end

%%
for s=1:size(V,3);
  Vfill(:,:,s)=imfill(Vclose(:,:,s),'holes');
end

%% Plots 3D of volume
V=Vfill;

figure
patch(isocaps(V,.5),'FaceColor','interp','EdgeColor','none');
p1 = patch(isosurface(V,.5),'FaceColor','red','EdgeColor','none');
isonormals(V,p1)
view(3);
axis vis3d tight
camlight right
lighting gouraud
```